On the Three-Particle Toda Lattice and Some of Its Approximants

Timo Hofmann

Leipzig University, FMI, PF 100920, D-04009 Leipzig
(E-mail: `hofmann13.th@googlemail.com`)

Abstract: In order to study the three-particle Toda-Hamiltonian and some of its approximants, we distinguish the central periodic orbits into two types (I) and (II): whether or not there is some time $t_1 > 0$ such that the kinetic energy of the system equals 0 at t_1. We start with a detailed investigation of the integrable, three-particle Toda-Hamiltonian and describe explicitly the stable, 1:1 periodic central obits o_i, $i = 1, 2$, which are of type (II). It is shown further that each point of the separatrix $\mathcal{S}(E)$ corresponds uniquely to an unstable, 1:1 periodic orbit of type (I), and two important families τ_j, σ_j, $j = 1, 2, 3$, of such orbits are described in detail.

In order to study the 4-th and 6-th order approximations H_4 and H_6 of the Toda-Hamiltonian, respectively, we consider the periodic orbits $\tau_j^{(k)}$, $\sigma_j^{(k)}$, $j = 1, 2, 3$, $k = 4, 6$, which are related to τ_j, σ_j. Solving numerically the Hamiltonian equations we construct the Poincaré-section at surface $x = 0$ for several energies and distinguish the regions of stability and non-stability of the above orbits with respect to the energy E of the system. Along these lines, we obtain that H_6 has two nearly separated chaotic seas for energies $16 \le E \le 16.2$ and two completely separated chaotic seas at energy $E = 35$.

Finally, we consider the Hamiltonian $\widetilde{H}_2$ whose potential is given by the difference of the potential of the Toda-Hamiltonian and its second order approximation. We show that there are three completely separated chaotic seas at energy $E = 12$.

Key words: Three-particle Toda-Hamiltonian, approximants of Toda-Hamiltonian, periodic orbits, bifurcation of trajectories, separated chaotic seas

1 Introduction

It is known that a typical Hamiltonian system has a phase space divided into KAM tori and chaotic sea(s) both of positive measure, see [11]. While the dynamics in KAM tori is regular that in chaotic sea(s) is chaotic. It was shown by Bunimovich that there are examples where an arbitrary number of islands with regular dynamics coexist with an arbitrary number of ergodic components with chaotic dynamics. Those results are also of some interest for statistical physics, see [4], [14] . All of the above examples are constructed as billiards in $\mathbb{R}^2$ with suitably chosen border, see [3], [15].

The aim of the present paper is to give two-dimensional examples of Hamiltonian systems with Hamiltonian

$$H = \frac{1}{2} \left(p_x^2 + p_y^2 \right) + V(x, y), \quad x, y \in \mathbb{R}, \tag{1}$$

and suitably chosen potential V such that for varying energies E of the system, we get similar properties as those of the above examples by Bunimovich. There are the systems with pure, extreme behaviors: either the purely integrable one where the phase space is fully foliated by invariant tori (e.g. Toda-Hamiltonian, see Fig. 3) or the purely non-integrable one, where it consists of just one ergodic component. Especially, we are interested in examples between those extremal ones with more than one chaotic sea.

After the pioneering paper by Hénon and Heiles ([8]), the n-th order truncations, $n \geq 3$, of the Hamiltonian of the three-particle Toda lattice were intensively studied, see [6], [18], [21], [22] [5, ch. 2.2.8]. Due to numerical calculations, there is the conjecture that there are two separated chaotic seas for H_6 at energy $E = 18$, see [22], [9]. However, those seas are not completely separated, and we achieved the most best results for energies $16 \leq E \leq 16.2$, where the empirical probability h for leaving one chaotic sea into the other one after $T = 30000$ time steps satisfies

$$6.56\% \leq h \leq 10\%, \tag{2}$$

see Fig. 23. In order to explain that phenomenon (2), we consider the central periodic orbits of the Toda Hamiltonian H and its approximants H_4, H_6 since they are the frame of those systems. Especially, their stability and non-stability, respectively, at different energies define the behavior of the system. Furthermore, we have to distinguish the central periodic orbits into two types (I), (II), whether or not there is some time t_1 at which the kinetic energy of the system equals 0, see (36) , (37). A final explanation of (2) based on the appearance of cantori will be given in Section 3.3. Further, we obtained two completely separated, chaotic seas (a big one and a small one) for H_6 at energy $E = 35$.

On the other hand, we achieved most interesting results for the Hamiltonian

$$\widetilde{H}_2 = \frac{1}{2} \left(p_x^2 + p_y^2 \right) + \widetilde{V}_2, \tag{3}$$

where $\widetilde{V}_2 = V - V_2$, V and V_2 denote the potential of the Toda Hamiltonian and its second order approximation, respectively. At low energy $E = 1$, there is only one big chaotic sea and only a very small regular island around stable periodic 2:2 orbits are visible. At the most interesting energy $E = 12$, there are several KAM tori and three completely separated chaotic seas. At high energy $E = 200$, the system is nearly regular. In a forthcoming paper we will investigate $\widetilde{H}_2$ in detail.

The paper is organized as follows. In Section 2 the three-particle Toda Hamiltonian is considered with emphasis on the separatrix $\mathcal{S}(E)$ and the central periodic orbits o_i, $i = 1, 2$, which play a prominent role for its approximants.

While the points on $\mathcal{S}(E)$ correspond to unstable periodic orbits of type (I), the orbits o_i are stable and of type (II). The projections of those orbits of type (I) into the (x, y)-plane will be considered in Proposition 1 and Remark 2, and approximations of them will be explicitly given in Remark 5. Using the second integral (26) of the Toda Hamiltonian, the orbits o_i will be explicitly characterized in Proposition 3.

Section 3 is devoted to some approximants of the Toda Hamiltonian H. The main feature is that the separatrix $\mathcal{S}(E)$ disappears and instead of it chaotic seas and KAM tori appear. Further, the periodic orbits $o_i^{(n)}$, $(i = 1, 2;\ n = 4, 6)$ of type (II), which correspond to o_i of the Toda Hamiltonian, are present and stable for almost all energies. Moreover, two families $\tau_j^{(n)}, \sigma_j^{(n)}$, $(j = 1, 2, 3;\ n = 4, 6)$, of periodic orbits of type (I) appear, see Proposition 4 , Remark 7. Their stability and non-stability, respectively, at different energies explain the differences between those approximants, see Sections 3.2, 3.3, 4. In Section 3.4, the Hamiltonian (3) will be considered.

2　The three-particle Toda lattice

2.1　Some definitions

We consider a periodic one-dimensional lattice with Hamiltonian

$$H = \frac{p_1^2}{2} + \frac{p_2^2}{2} + \frac{p_3^2}{2} + e^{-(q_1-q_2)} + e^{-(q_2-q_3)} + e^{-(q_3-q_1)} - 3\,, \qquad (4)$$

where q_i and p_i are the positions and momenta of the three particles, $i = 1, 2, 3$, see [13, p. 22],[17, Sec. 1.1]. This system describes a chain of three particles moving along a straight line, and the neighboring particles are coupled by non-linear springs, see [7, p. 41].
The Hamiltonian (4) is reduced to that of a two-dimensional system

$$H = \frac{1}{2}\left(p_x^2 + p_y^2\right) + \frac{1}{24}\left(e^{(2\sqrt{3}x+2y)} + e^{(-2\sqrt{3}x+2y)} + e^{-4y}\right) - \frac{1}{8} \qquad (5)$$

by a canonical transformation due to Lansford, Ford,[10], see also [5], [17, Sec. 1.2]. A contour plot and some streamlines of the Toda potential

$$V = \frac{1}{24}\left(e^{(2\sqrt{3}x+2y)} + e^{(-2\sqrt{3}x+2y)} + e^{-4y}\right) - \frac{1}{8} \qquad (6)$$

of the above Hamiltonian (5) are illustrated in Fig. 1. In the $(x, y)-$plane, the zero velocity curve (ZVC) for energy $E > 0$ is given by

$$\mathcal{Z}(E) = \{(x, y) \in \mathbb{R}^2 \,|\, V(x, y) = E\}. \qquad (7)$$
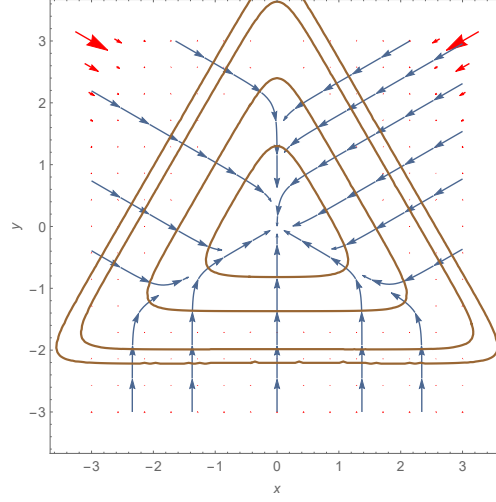
Fig. 1. Equi-potential (brown), $-\nabla V$ (red) and stream (blue) lines of the Toda potential (6).

For the following, let us put

$$\eta = \sqrt{8E+1} \tag{8}$$

for energy $E > 0$.

Lemma 1. a) *The equi-potential curves of the Toda potential for energy $E > 0$ are explicitly given by*

$$y_1 = \Phi(x; E) = -\frac{1}{2} \log\left(-2\eta \, \cos\left(\frac{1}{3} \arccos\left(-\eta^{-3} \cosh(2\sqrt{3}\,x)\right) + \frac{\pi}{3}\right)\right) \tag{9}$$

$$y_2 = \Psi(x; E) = -\frac{1}{2} \log\left(2\eta \, \cos\left(\frac{1}{3} \arccos\left(-\eta^{-3} \cosh(2\sqrt{3}\,x)\right)\right)\right) \tag{10}$$

with $-x_0 \leq x \leq x_0$, where

$$x_0 = \frac{\operatorname{arcosh}\left(\eta^3\right)}{2\sqrt{3}}\,. \tag{11}$$

b) *The curve*

$$y_3 = \Theta(x; E) = -\frac{1}{2} \log\left(\eta \, \cos\left(\frac{1}{3} \arccos\left(\eta^{-3} \cosh(2\sqrt{3}\,x)\right)\right)\right) \tag{12}$$

satisfies

$$\Psi(x; E) < \Theta(x; E) < \Phi(x; E) \tag{13}$$

for $-x_0 < x < x_0$, and

$$\Psi(x_0; E) = \Psi(-x_0; E) = \Phi(x_0; E) = \Phi(-x_0; E) = \Theta(x_0; E) =$$
$$= \Theta(-x_0; E) = -\frac{1}{2} \, \log \eta, \tag{14}$$

see Fig. 2.

Proof. a) We set

$$z = e^{-2y}.$$ (15)

Then, (6) yields

$$\frac{1}{24}\left(\frac{2\cosh\left(2\sqrt{3}x\right)}{z} + z^2 - \frac{1}{8}\right) = E$$

$$\Leftrightarrow z^3 - (24E+3)z + 2\cosh\left(2\sqrt{3}\,x\right) = 0$$

$$\stackrel{(8)}{\Leftrightarrow} z^3 - 3\eta^2 z + 2\cosh\left(2\sqrt{3}\,x\right) = 0$$ (16)

For energy $E > 0$ the casus irreducibilis applies to (16), and the formula of Cardano yields

$$z_1 = -2\eta\ \cos\left(\frac{1}{3}\arccos\left(-\eta^{-3}\cosh(2\sqrt{3}\,x)\right) + \frac{\pi}{3}\right),$$ (17)

$$z_2 = 2\eta\ \cos\left(\frac{1}{3}\arccos\left(-\eta^{-3}\cosh(2\sqrt{3}\,x)\right)\right)$$ (18)

$$z_3 = -2\eta\ \cos\left(\frac{1}{3}\arccos\left(-\eta^{-3}\cosh(2\sqrt{3}\,x)\right) - \frac{\pi}{3}\right),$$ (19)

and it follows $z_1 > 0$, $z_2 > 0$, $z_3 < 0$. Now, (15), (17), (18) imply (9), (10). Set

$$u = \frac{\cosh(2\sqrt{3}\,x)}{\eta^3}.$$ (20)

Noticing that $|u| \leq 1$ iff $-x_0 \leq x \leq x_0$, we infer that $\Phi(x;E) \in \mathbb{R}$, $\Psi(x;E) \in \mathbb{R}$ iff $-x_0 \leq x \leq x_0$.

b) (14) follows straightforward by inserting $x = x_0$ and $x = -x_0$ in (9), (10), (12).

Since $\cosh(\cdot)$ is an even function, the functions $\Phi(x;E)$, $\Psi(x;E)$, $\Theta(x;E)$ are also even with respect to x. It is straightforward to check that $\Phi(x;E)$, $\Theta(x;E)$ are strictly monotonically decreasing and $\Psi(x;E)$ is strictly monotonically increasing for $0 \leq x \leq x_0$. Due to (14) and the symmetry of the functions under consideration, we get

$$\Psi(x;E) < \Theta(x;E)$$ (21)

for $-x_0 < x < x_0$. Using (20), we consider the difference

$$f(u) = \cos\left(\frac{1}{3}\arccos(u)\right) - 2\cos\left(\frac{1}{3}\arccos(-u) + \frac{\pi}{3}\right)$$

$$= \cos\left(\frac{1}{3}\arccos(u)\right) - 2\sin\left(\frac{1}{3}\arcsin(u)\right).$$ (22)

Then

$$\frac{df}{dx} = \frac{df}{du}\cdot\frac{du}{dx} = \frac{\sin\left(\frac{1}{3}\arccos(u)\right) - 2\cos\left(\frac{1}{3}\arcsin(u)\right)}{3\sqrt{1-u^2}}\cdot\frac{du}{dx}$$ (23)

follows. Noticing

$$0 \leq \sin\left(\frac{1}{3}\arccos(u)\right) \leq \frac{1}{2}$$

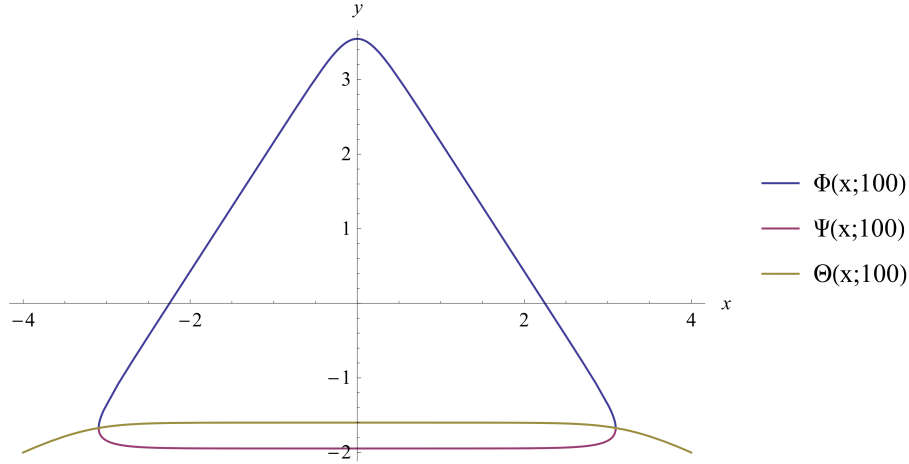$$-2 \leq -2\cos\left(\frac{1}{3}\arcsin(u)\right) \leq -\sqrt{3}$$

$$0 < 3\sqrt{1-u^2},$$

we get $\frac{df}{du} < 0$ for $0 \leq x \leq x_0$. Since $u(x)$ is strictly monotonically increasing for $0 \leq x \leq x_0$, it follows $\frac{du}{dx} > 0$, and then $\frac{df}{dx} < 0$ for $0 \leq x \leq x_0$. Since $u(x_0) = 1$, we get

$$f(x) > f(x_0) = 0 \tag{24}$$

for $0 \leq x < x_0$. Hence,

$$\cos\left(\frac{1}{3}\arccos(u)\right) > -2\cos\left(\frac{1}{3}\arccos(-u) + \frac{\pi}{3}\right), \tag{25}$$

and then $\Theta(x; E) < \Phi(x; E)$ for $0 \leq x < x_0$ follows. Using (21) and the symmetry of Φ and Θ, we get (13).

Fig. 2. The zero velocity curve (ZVC) of the Toda potential (6) at Energy $E = 100$. Blue and purple curve are $y_1(x) = \Phi(x, 100)$ and $y_2(x) = \Psi(x, 100)$, respectively, see (9), (10). The curve $\Theta(x; 100)$ is estimated by using complex numbers, and thus it is defined for $x \in \mathbb{R}$.

Remark 1. **a)** It is well-known that the Toda lattice is an integrable system, and a second integral is given by

$$I(x, p_x, y, p_y) = 8p_x^3 - 24p_x p_y^2 + p_x\left(e^{2(y+\sqrt{3}x)} + e^{2(y-\sqrt{3}x)} - 2e^{-4y}\right)$$
$$-\sqrt{3}p_y\left(e^{2(y+\sqrt{3}x)} - e^{2(y-\sqrt{3}x)}\right) \tag{26}$$

(see [5, Sec. 2.2.8].)

b) The general form of the n-th truncated Hamiltonian is given by $H_n = \frac{1}{2}\left(p_x^2 + p_y^2\right) + V_n(x,y)$, where $V_n(x,y)$ is the n-order approximation of the Toda potential (6). It is well-known that H_2 (the superposition of two independent harmonic oscillators) is integrable, but all the other H_n with $n > 2$ are non-integrable, see [20].

Using the integral (26), we can construct the Poincaré-section for the surface $x = 0$ without solving the Hamiltonian system of differential equations. Considering

$$F(y,p_y) := I\left(0, \sqrt{2E - 2V(0,y) - p_y^2}, y, p_y\right)$$

$$= I\left(0, \sqrt{2E - \frac{1}{12}\left(2e^{2y} + e^{-4y}\right) + \frac{1}{4} - p_y^2}, y, p_y\right)$$

$$= \sqrt{2E - \frac{1}{12}\left(2e^{2y} + e^{-4y}\right) + \frac{1}{4} - p_y^2}$$

$$\cdot \left(8E + \frac{1}{3}e^{2y} - \frac{4}{3}e^{-4y} - 16p_y^2 + 1\right)$$

$$\overset{(8)}{=} \sqrt{\frac{\eta^2}{4} - \frac{1}{12}\left(2e^{2y} + e^{-4y}\right) - p_y^2}$$

$$\cdot \left(\eta^2 + \frac{1}{3}e^{2y} - \frac{4}{3}e^{-4y} - 16p_y^2\right) \tag{27}$$

we get the Poincaré-section for energy $E > 0$ by setting

$$F(y,p_y) = c, \tag{28}$$

where the constants $c \in \mathbb{R}$ refer to different initial values, see [5, Sec. 2.5.2]. For each energy $E > 0$, the Poincaré-sections look similar, see Fig. 3. The inner of the limiting curve of the Poincaré-section is completely filled with invariant curves which are the intersections of regular tori with the plane $x = 0$. Both parts of the invariant curves are separated by the separatrix $F(y,p_y) = 0$. If

$$p_x = \sqrt{\frac{\eta^2}{4} - \frac{1}{12}\left(2e^{2y} + e^{-4y}\right) - p_y^2} \neq 0, \tag{29}$$

(27) yields $\eta^2 + \frac{1}{3}e^{2y} - \frac{4}{3}e^{-4y} - 16p_y^2 = 0$, and then

$$p_y = \pm\frac{1}{4}\sqrt{\eta^2 + \frac{1}{3}e^{2y} - \frac{4}{3}e^{-4y}}. \tag{30}$$

Solving $p_y = 0$ in (30) and using (15), we get the cubic equation

$$z^3 - \frac{3\eta^2}{4}z - \frac{1}{4} = 0 \tag{31}$$

and the casus irreducibilies applies to (31) for $E > 0$. The only solution of (31) bigger than zero is given by

$$z(E) = \eta \, \cos\left(\frac{1}{3} \arccos\left(\eta^{-3}\right)\right) , \tag{32}$$

and then

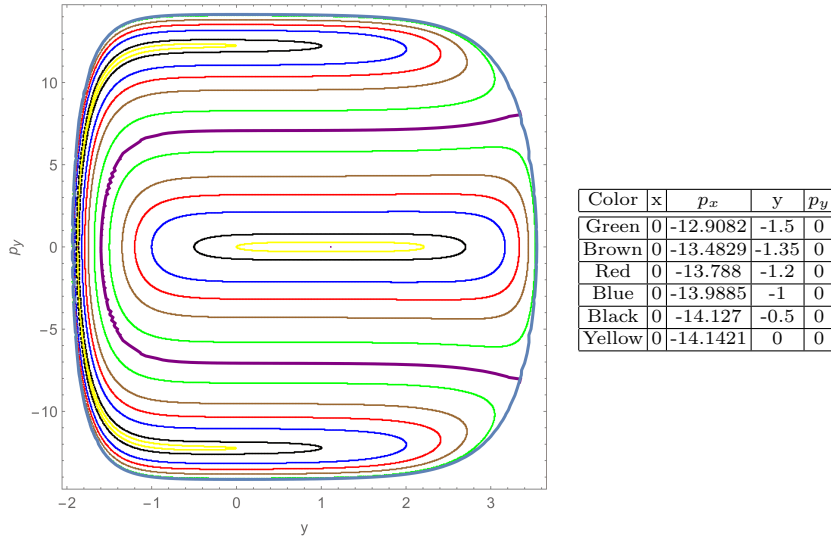$$y_s(E) = -\frac{1}{2} \, \ln(z(E)) \tag{33}$$

follows. For the separatrix we get

$$\mathcal{S}(E) = \left\{ (y, p_y) \in \mathbb{R}^2 \,\middle|\, p_y = \pm\frac{1}{4}\sqrt{\eta^2 + \frac{1}{3}e^{2y} - \frac{4}{3}e^{-4y}}, \right.$$

$$\left. y_s(E) \le y \le \Phi(0, E) \right\} , \tag{34}$$

where $(y_s(E), 0)$ is the apex of $\mathcal{S}(E)$. Furthermore, let

$$\mathcal{S}_1(E) = \mathcal{S}(E) \setminus \left\{ \left(\Phi(0; E); -\frac{1}{4}\sqrt{\eta^2 + \frac{1}{3}e^{2\Phi(0;E)} - \frac{4}{3}e^{-4\Phi(0;E)}} \right) \right\}, \tag{35}$$

i.e., the two yellow points of the separatrix in Fig. 4 that intersect the limiting curve are identified in $\mathcal{S}_1(E)$.

Color	x	p_x	y	p_y
Green	0	-12.9082	-1.5	0
Brown	0	-13.4829	-1.35	0
Red	0	-13.788	-1.2	0
Blue	0	-13.9885	-1	0
Black	0	-14.127	-0.5	0
Yellow	0	-14.1421	0	0

Fig. 3. Poincaré-section of the Toda-Hamiltonian (5) at surface $x = 0$ for energy $E = 100$. The separatrix $F(y, p_y) = 0$ and the limiting curve $p_x = 0$ are given by the thick purple and the thick blue curve, respectively. The initial values of the considered orbits are given in the above table. The central orbit is the purple point at $y \approx 1.10974$, $p_y = 0$. The second point of that central orbit in the Poincaré-section is not visible.
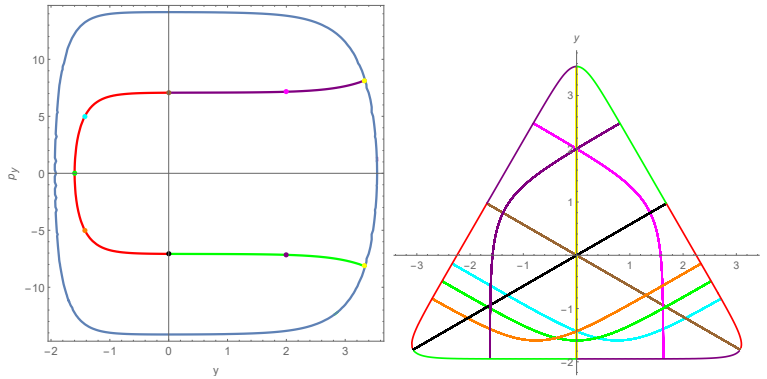
Fig. 4. The separatrix of the Toda-Hamiltonian for energy $E = 100$ is the union of the purple, red and green curve in the (y, p_y)-plane in the above first figure. The limiting curve is given by the blue curve. The second figure shows the ZVC that is the union of the purple, red and green parts of the surrounding curve. Furthermore, eight 1:1 resonance orbits are shown, where the color corresponds to the color of the points at the separatrix shown in the first figure.
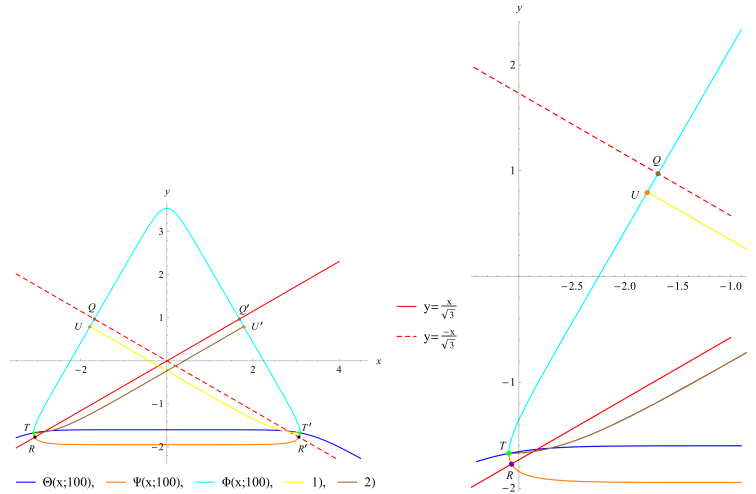
Fig. 5. The intersection points $R, T, U, Q, R', T', U', Q'$ at the ZVC are given for $E = 100$. The initial values of the yellow and brown trajectories are 1) $\{x(0), p_x(0), y(0), p_y(0)\} = \{3.09516, 0, -1.67147, 0\}$ and 2) $\{x(0), p_x(0), y(0), p_y(0)\} = \{-3.09516, 0, -1.67147, 0\}$, respectively.

2.2 Periodic orbits

There are two kinds of periodic orbits concerning their initial values:

$$(I): \text{ there is some time } t_1 \text{ such that } p_x(t_1)^2 + p_y(t_1)^2 = 0\,, \qquad (36)$$

$$(II): p_x(t)^2 + p_y(t)^2 > 0,\ \forall t > 0. \qquad (37)$$

Case (I) Let us introduce some special points on the ZVC, see Fig. 5 . Let $T(t_x, t_y)$ and $T'(t'_x, t'_y)$ denote the intersection points of the curves $\Phi(\cdot; E)$, $\Psi(\cdot; E)$, $\Theta(\cdot; E)$. Lemma 1 b) implies

$$t_x = -t'_x \overset{(11)}{=} \frac{\operatorname{arcosh}\left(\eta^3\right)}{2\sqrt{3}}, \tag{38}$$

$$t_y = t'_y \overset{(14)}{=} -\frac{1}{2}\log\eta. \tag{39}$$

Further let $R(r_x, r_y)$ and $Q'(q'_x, q'_y)$ (respectively $R'(r'_x, r'_y)$ and $Q(q_x, q_y)$ denote the intersection points of the ZVC with the straight line $y = \frac{x}{\sqrt{3}}$ (respectively $y = -\frac{x}{\sqrt{3}}$). Finally, let $U(u_x, u_y)$ and $U'(u'_x, u'_y)$ denote those points on the ZVC which will be reached by trajectories with initial values $x(0) = t_x$, $p_x(0) = 0$, $y(0) = t_y$, $p_y(0) = 0$ and $x(0) = -t_x$, $p_x(0) = 0$, $y(0) = t_y, p_y(0) = 0$, respectively.

The trajectories satisfying (I) are considered in the (x, y)-plane in the following proposition.

Proposition 1. *The three straight lines*

$$y_1 = \frac{x}{\sqrt{3}}, \quad r_x \le x \le q'_x, \tag{40}$$

$$y_2 = -\frac{x}{\sqrt{3}}, \quad q_x \le x \le r'_x, \tag{41}$$

$$x = 0, \quad y_{min} \le y_3 \le y_{max}, \tag{42}$$

are 1:1 resonance orbits of the Toda-Hamiltonian (5) *for Energy* $E > 0$*, which correspond to the black, brown and yellow curve in Fig. 4, respectively, where*

$$y_{min} = -\frac{1}{2}\log\left(2\eta\cos\left(\frac{1}{3}\arccos\left(-\eta^{-3}\right)\right)\right), \tag{43}$$

$$y_{max} = -\frac{1}{2}\log\left(-2\eta\cos\left(\frac{\pi}{3} + \frac{1}{3}\arccos\left(-\eta^{-3}\right)\right)\right), \tag{44}$$

$$r_x = -r'_x = -\frac{\sqrt{3}}{2}\cdot y_{max}, \tag{45}$$

$$q'_x = -q_x = -\frac{\sqrt{3}}{2}\cdot y_{min}. \tag{46}$$

Proof. For the gradient of the potential (6), it follows

$$(\nabla V)(0, y) = \frac{1}{6}\begin{pmatrix} 0 \\ -e^{-4y} + e^{2y} \end{pmatrix}, \tag{47}$$

and thus (42) follows. Since $y_{min} = \Psi(0, E)$, $y_{max} = \Phi(0, E)$, we get (43), (44). Using the argument of Remark 4, the assertions follow for (40), (41), (45), (46), too.

Remark 2. The 1:1 resonance orbits that connect the two red parts of the ZVC in Fig. 4 are given by a family of curves $y_\alpha(x; E)$, where the indexes α refer
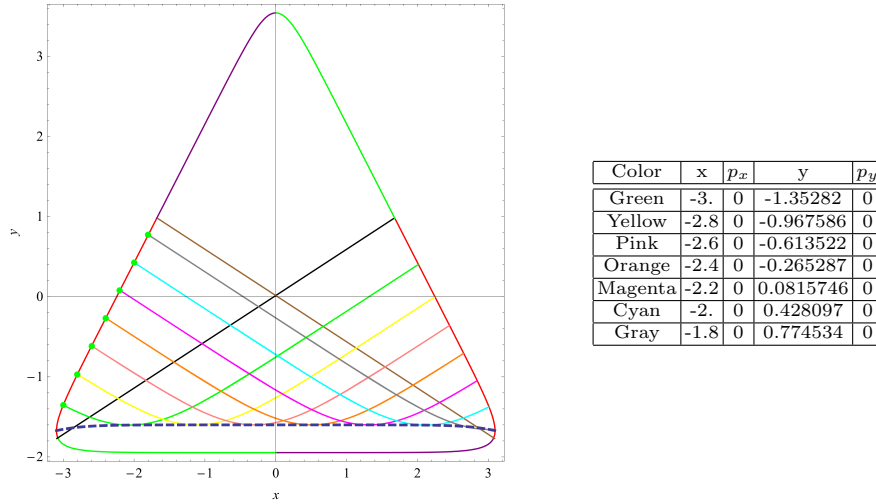
to the ordinates of the intersection points of the trajectories with the left part $(x \leq 0)$ of the ZVC, and it holds

$$r_y \leq \alpha \leq q_y. \qquad (48)$$

We numerically solved the Hamiltonian system of four differential equations

$$\dot{x} = \frac{\partial H}{\partial p_x}, \quad \dot{y} = \frac{\partial H}{\partial p_y}, \quad \dot{p}_x = -\frac{\partial H}{\partial x}, \quad \dot{p}_y = -\frac{\partial H}{\partial y}$$

by the symplectic partitioned Runge-Kutta method of difference order 8 (see [19], [16]), where H is taken from (5). Some orbits starting at the red part of the ZVC are shown in Fig. 6.

Color	x	p_x	y	p_y
Green	-3.	0	-1.35282	0
Yellow	-2.8	0	-0.967586	0
Pink	-2.6	0	-0.613522	0
Orange	-2.4	0	-0.265287	0
Magenta	-2.2	0	0.0815746	0
Cyan	-2.	0	0.428097	0
Gray	-1.8	0	0.774534	0

Fig. 6. The above figure shows the ZVC for energy $E = 100$ in red, green and purple color. The straight lines (40), (41) are in black and brown, respectively. Some further 1:1 resonance orbits that connect the red parts of the ZVC are shown, where the initial values are given in the above table and indicated by green points on the ZVC. The curve of apexes (50) is shown as the blue dashed curve.

Proposition 2. *The trajectories $y_\alpha(x; E)$ with $t_y \leq \alpha \leq u_y$ are curves with apexes $S^{(\alpha)}(s_x^{(\alpha)}, s_y^{(\alpha)})$, i.e.,*

$$\frac{\mathrm{d}y_\alpha}{\mathrm{d}x}(s_x^{(\alpha)}) = 0, \qquad (49)$$

cf. Remark 5. The coordinates of the apexes $S^{(\alpha)}(s_x^{(\alpha)}, s_y^{(\alpha)})$ satisfy

$$s_y^{(\alpha)} = \Theta(s_x^{(\alpha)}; E). \qquad (50)$$

Proof. For the apexes, we have

$$p_y = 0 \qquad (51)$$

$$p_x \neq 0. \qquad (52)$$

Using (51) and that the Hamiltonian (5) is an integral, we get by setting $H = E$:

$$p_x = \pm \frac{\sqrt{3\eta^2 - e^{-4y} - e^{-2\sqrt{3}x+2y} - e^{2\sqrt{3}x+2y}}}{2\sqrt{3}} \tag{53}$$

Without loss of generality we only consider the case "+-case" since due to symmetry the trajectory moves in both directions (forward and backward). Inserting

$$z = e^{-2y}, \tag{54}$$

the "+-case" of (53) and (51) into (26) and using that the separatrix is given by $I(x, p_x, y, p_y) = 0$, we get

$$\frac{\left(z(3\eta^2 - 4z^2) + \cosh\left(2\sqrt{3}x\right)\right) \cdot \sqrt{9\eta^2 - 3z^2 - \frac{6\cosh\left(2\sqrt{3}x\right)}{z}}}{9z} = 0 \tag{55}$$

Setting the first factor of the numerator of (55) equally to zero, we get the cubic equation

$$z^3 - \frac{3\eta^2}{4}z - \frac{1}{4}\cosh\left(2\sqrt{3}\,x\right) = 0 \tag{56}$$

in z. For $E > 0$ the casus irreducibilis applies. The only solution of (56) for $x = 0$, which is bigger than zero, is given by

$$z = \eta \cos\left(\frac{1}{3}\arccos\left(\eta^{-3}\cosh\left(2\sqrt{3}\,x\right)\right)\right). \tag{57}$$

Using (54) and (12), we get (50), see Fig. 6.
If the second factor of (55) equals zero, we get the cubic equation (31) with solutions (9), (10) by Lemma 1. But in this case we have $p_x = p_y = 0$, and thus those solutions do not represent apexes.

Remark 3. The 1:1 resonance orbits which start at ZVC between R and T reach the ZVC again between U' and Q', and those orbits which start at ZVC between U and Q reach the ZVC again between R' and T', see Fig. 5.

Remark 4. Since the Toda-potential (6) is symmetric with respect to rotations around $\frac{2}{3}\pi$ and $\frac{4}{3}\pi$, the corresponding assertions of Remark 2 and Proposition 2 apply to the green and purple part of the ZVC in Fig. 4, too.

Remark 5. Good approximations of the curves $y_\alpha(x)$, $t_y \leq \alpha \leq u_y$, considered in Remark 2 are given by

$$\widetilde{y}_\alpha(x; E) = \begin{cases} -\Phi(\omega_1(x - s_x), E) + \Phi(0, E) + s_y, & x \leq s_x \\ -\Phi(\omega_2(x - s_x), E) + \Phi(0, E) + s_y, & x \geq s_x \end{cases} \tag{58}$$

where (s_x, s_y) denote the coordinates of the apex of the orbit, i.e. $p_y(s_x, s_y) = 0$, and $\omega_i, i = 1, 2$, are suitable chosen factors, such that the orbit perpenticularly cuts the ZVC, see Fig. 6.

The factors ω_i, $i = 1, 2$, are numerically estimated with accuracy of 10^{-13} by regula falsi. In Table 1, the factors ω_1, the differences $\omega_2 - \omega_1$ and the L_2-norms of differences $\|y_\alpha(\cdot; E) - \widetilde{y}_\alpha(\cdot; E)\|_2$ are given for some apexes $S(s_x, s_y)$ and energy $E = 100$. In Fig. 7, some curves y_α, $\widetilde{y}_\alpha$ are shown for energy $E = 100$. In Fig. 8 the difference $y_\alpha - \widetilde{y}_\alpha$ is shown over three time steps for an example of initial values.

Table 1

s_x	0.	0.5	1.	1.5	2.	2.5	2.8
s_y	-1.59955	-1.59956	-1.59961	-1.59993	-1.60169	-1.61123	-1.63015
ω_1	0.333333	0.333333	0.333333	0.333333	0.333333	0.333332	0.333331
$\omega_2 - \omega_1$	0.	$3.22 \cdot 10^{-8}$	$9.03 \cdot 10^{-8}$	$2.2 \cdot 10^{-7}$	$5.27 \cdot 10^{-7}$	$1.27 \cdot 10^{-6}$	0.112171
$\|y_\alpha - \widetilde{y}_\alpha\|_2$	$3.8 \cdot 10^{-8}$	$9.7 \cdot 10^{-7}$	$2.5 \cdot 10^{-7}$	$6.7 \cdot 10^{-7}$	$1.8 \cdot 10^{-6}$	$5 \cdot 10^{-6}$	$9 \cdot 10^{-6}$

$\Theta(x;100), \quad \Psi(x;100), \quad \Phi(x;100),$
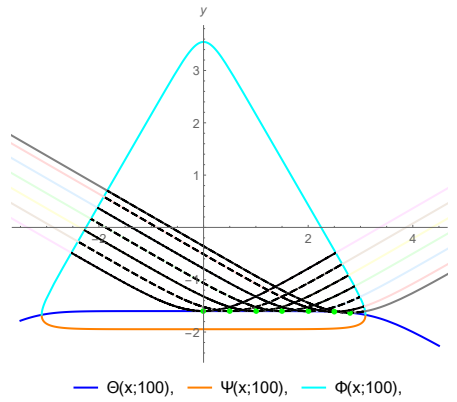
Fig. 7. The curves y_α are numerically estimated by by the symplectic partitioned Runge-Kutta method of difference order 8, see Remark 2, and shown by black dashed lines for initial values taken from Table 1 and indicated by green points. Furthermore, the curves $\widetilde{y}_\alpha$ are estimated by (58) and shown in the colors light magenta, light brown, light yellow, light green light blue, light red and grey, where the values of s_x, s_y, ω_i, $i = 1, 2$, are taken from Table 1.
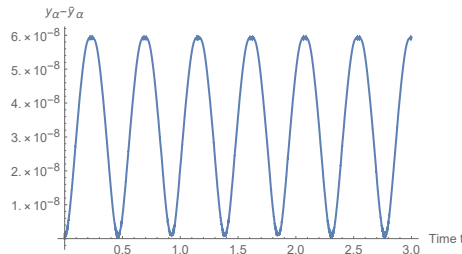
Fig. 8. The difference $y_\alpha - \widetilde{y}_\alpha$ is shown over three time steps for initial values $x(0) = 0, y(0) = -1.9955, p_y(0) = 0, E = 100$.

Furthermore, let $\mathcal{M}(E)$ denote the set of all 1:1 resonance orbits satisfying property (I) for given energy E. Finally, let

$$\mathcal{Z}_1(E) = \{(x,y) \in \mathcal{Z}(E) \,|\, x < 0\} \cup \{(x,y) \in \mathbb{R}^2 \,|\, V(0,y) = E,\, y > 0\} \quad (59)$$

denote the left half of ZVC (see (7)), where the two points of the ZVC that are on the y-axes are identified, i.e. curves of the same color are identified in Fig. 4.

The main results of the present subsection are summarized in the following.

Corollary 1. *There are two bijections* $\chi_1 : \mathcal{Z}_1(E) \to \mathcal{M}(E)$ *and* $\chi_2 : \mathcal{M}(E) \to \mathcal{S}_1(E)$.

Proof. Using Proposition 1 and Remarks 2, 3, 4 , we get that every point $P \in \mathcal{Z}_1(E)$ defines uniquely one element of $\mathcal{M}(E)$ by considering the orbit with initial values defined by P. Vice verse, every 1:1 resonance orbit satisfying property (I) $o \in \mathcal{M}(E)$ reaches the ZVC at two points P_i, $i = 1, 2$, but exactly one of those points is in $\mathcal{Z}_1(E)$. Hence χ_1 is a bijection. The bijection χ_2 follows from Fig. 4.

Let us introduce the following notations.

Definition 1. Let the three trajectories considered in (40), (41), (42) denoted by τ_j, $j = 1, 2, 3$. Furthermore, let σ_1 denote the trajectory $y_{\alpha_0}(x; E)$ defined in Remark 2, where α_0 is chosen such that $s_x^{(\alpha_0)} = 0$ applies. Let $\sigma_{2,3}$ denote rotations of σ_1 around $\frac{2}{3}\pi$ and $\frac{4}{3}\pi$, respectively.

Case (II) In the case under consideration the periodic orbits never reach the ZVC. Of special interest are both central periodic 1:1 orbits. The projections of them into the (x, y)-plane coincide, where one of them moves clockwise while the other moves anti-clockwise, see Fig. 9.

Proposition 3. a) *The two central periodic 1:1 orbits* o_i, $i = 1, 2$, *are explicitly given by*

$$o_i : x = g(y),\; \boldsymbol{p} = \begin{pmatrix} p_x \\ p_y \end{pmatrix} = \lambda_i(y) \begin{pmatrix} a \\ 1 \end{pmatrix}, \quad (60)$$

$$x = -g(y),\; \boldsymbol{p} = \begin{pmatrix} p_x \\ p_y \end{pmatrix} = -\lambda_i(y) \begin{pmatrix} a \\ 1 \end{pmatrix}, \quad (61)$$

where

$$g(y) = \frac{1}{\sqrt{3}} \log\left(\frac{\sqrt{-\sqrt{9\eta^2 \mathrm{e}^{4y} - 6\eta \mathrm{e}^{8y} + \mathrm{e}^{12y} - 4} + 3\eta \mathrm{e}^{2y} - \mathrm{e}^{6y}}}{\sqrt{2}} \right), \quad (62)$$

$$\lambda_{1,2}(y) = \pm \frac{\mathrm{e}^{-2y}}{4\sqrt{3}} \cdot \sqrt{\mathrm{e}^{4y}\left(\mathrm{e}^{4y} - 3\eta\right)^2 - 4}, \quad (63)$$

$$a = \frac{\sqrt{3}\mathrm{e}^{2y}\left(\mathrm{e}^{4y} - \eta\right)}{\sqrt{\mathrm{e}^{4y}\left(\mathrm{e}^{4y} - 3\eta\right)^2 - 4}}, \quad (64)$$

and η is taken from (8)

b) *The projections of both central 1:1 orbits are implicitly given by*

$$e^{-2\sqrt{3}\,x-2y} + e^{2\sqrt{3}\,x-2y} + e^{4y} = 3\eta \tag{65}$$

in the (x,y)-plane.

c) *In the Poincaré-Section at surface $x = 0$, the orbit considered in a) defines two points $Q^{(1,2)}$, where their coordinates are given by*

$$Q^{(1)} : Q^{(1)}_y = \frac{1}{2} \log\left[2\sqrt{\eta}\,\cos\left(\frac{1}{3}\arccos\left(-\eta^{-3/2}\right)\right)\right],\; Q^{(1)}_{p_y} = 0, \tag{66}$$

$$Q^{(2)} : Q^{(2)}_y = \frac{1}{2} \log\left[-2\sqrt{\eta}\,\cos\left(\frac{1}{3}\arccos\left(-\eta^{-3/2}\right) + \frac{\pi}{3}\right)\right],$$

$$Q^{(2)}_{p_y} = 0. \tag{67}$$

Proof. a) The momentum $\boldsymbol{p}$ along the curve $x = g(y)$ satisfies

$$\boldsymbol{p} = \begin{pmatrix} p_x \\ p_y \end{pmatrix} = \lambda(y)\begin{pmatrix} \frac{\mathrm{d}g}{\mathrm{d}y} \\ 1 \end{pmatrix}, \tag{68}$$

where $\lambda(y)$ denotes a factor that will considered later. Since

$$\frac{\mathrm{d}g}{\mathrm{d}y} = \frac{\sqrt{3}e^{2y}\left(e^{4y} - \eta\right)}{\sqrt{e^{4y}\left(e^{4y} - 3\eta\right)^2 - 4}}, \tag{69}$$

(64) follows. Inserting (69), (68) in the Hamiltonian (5), we get

$$H(\lambda(y), y) = \frac{1}{24}\left(-\frac{36\lambda^2\left(\eta e^{2y} - 1\right)^2}{-3\eta e^{2y} + e^{6y} + 2} + 48\lambda^2 + \frac{36\left(\lambda\eta e^{2y} + \lambda\right)^2}{-3\eta e^{2y} + e^{6y} - 2}\right.$$

$$\left. +3\eta e^{4y} + e^{-4y} - e^{8y} - 3\right) \tag{70}$$

Since the Hamiltonian is an integral too, (70) yields for $H = E$ the functions $\lambda_i(y), i = 1, 2$:

$$\lambda_{1,2}(y) = \pm\frac{e^{-2y}}{4\sqrt{3}} \cdot \sqrt{e^{4y}\left(e^{4y} - 3\eta\right)^2 - 4},$$

and consequently, (63) follows. Inserting (60), (61) into the integral (26), we get

$$I_i(y) = \pm\left(\eta^3 - 1\right). \tag{71}$$

Hence H and I_i, $i = 1, 2$, are preserved along the orbits under consideration. Since the Hamiltonian H is conservative, a) follows.

b) Considering the projections of the orbits o_i, $i = 1, 2$, into the (x, y)-plane, we get

$$x = \begin{cases} g(y) \\ -g(y) \end{cases} \tag{72}$$

Since (65) is equivalent to (72), b) follows.

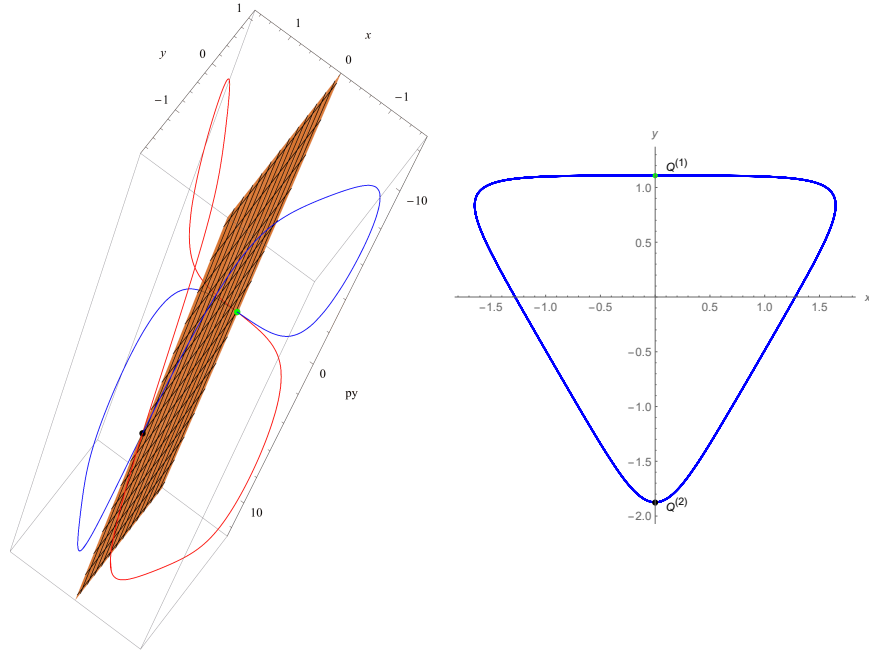*c)* Inserting $x = 0$, (8) and (15) in (65), we get the cubic equation

$$z^3 - 3\eta z + 2 = 0. \tag{73}$$

The casus irreducibilis applies to (73) for $E > 0$, and we get two solutions bigger than zero:

$$z_1 = 2\sqrt{\eta}\cos\left(\frac{1}{3}\arccos\left(-\eta^{-3/2}\right)\right), \tag{74}$$

$$z_2 = -2\sqrt{\eta}\cos\left(\frac{1}{3}\arccos\left(-\eta^{-3/2}\right) + \frac{\pi}{3}\right). \tag{75}$$

Using (6), we infer (66), (67).

Fig. 9. 3D-plot of the central 1:1 periodic orbits o_i, $i = 1, 2$, of the Toda-Hamiltonion for energy $E = 100$ and their projections into (x, y)-plane. In the left picture, the red and blue trajectories belong to the initial values $\{x(0), p_x(0), y(0), p_y(0)\} = \{0, 14.097, 1.11, 0\}$ and $\{x(0), p_x(0), y(0), p_y(0)\} = \{0, -14.097, 1.11, 0\}$, respectively. The green and black point are the two points $Q^{(1)}(1.11; 0)$ and $Q^{(2)}(-1.874; 0)$ visible in the Poincaré - section at surface $x = 0$, respectively (see (66), (67)). The surface $x = 0$ is shown in yellow. The right-hand picture represents the projections of the two orbits of the left-hand picture into (x, y)-plane.

Immediate consequences of the above are the following.

Corollary 2. a) *For each energy $E > 0$, the central periodic orbit considered in Proposition 3 exists.*
  b) *For both orbits o_i, $i = 1, 2$, the constant values of both integrals are given by*

$$H = E \tag{76}$$
$$I_i = \pm \left(\eta^3 - 1 \right), \tag{77}$$

where η is taken from (8).

Proof. a) Since $\eta > 1$ for $E > 0$, a) follows from (65).
  b) (71) implies (77).

Remark 6. Considering the potential

$$U(y) = V(g(y), y), \tag{78}$$

we get the solution $y(t)$, where g is taken from (62), see [2, §12], [10, Sec. 1.3a].

3 Some approximants of Toda-Hamiltonian H

In this section some approximants of the Toda-Hamiltonian will be investigated with focus on the existence of different chaotic seas.

3.1 Some general properties

Let V_n denote the Taylor-approximation of order n of the Toda-potential V (see (6)) around $(0,0)$, and $H_n = \frac{1}{2} \left(p_x^2 + p_y^2 \right) + V_n$ the corresponding Toda-Hamiltonian, $n \geq 2$. We also consider the differences

$$\widetilde{V}_n(x, y) = V(x, y) - V_n(x, y) \tag{79}$$

and the corresponding Hamiltonian $\widetilde{H}_n = \frac{1}{2} \left(p_x^2 + p_y^2 \right) + \widetilde{V}_n$, $n \geq 2$.
  It is well-known (see [21], [22]) that

(i) V_n and consequently $\widetilde{V}_n$ are symmetric with respect to rotations around $\frac{2}{3}\pi$ and $\frac{4}{3}\pi$.
(ii) For odd order n, there is a certain escape energy $E_n^{(esc)}$ for H_n, i.e., if the energy E of the system under consideration satisfies $E > E_n^{(esc)}$ then it is possible that some trajectories escape to infinity.
(iii) For even order n, there is no escape energy for H_n, i.e., for each energy E of the system, the trajectories remain in some bounded region.
(iv) For $\widetilde{H}_n$, there is no escape energy, $n \geq 2$.

Analogously to (7), we consider the ZVC's

$$\mathcal{Z}_n(E) = \{(x,y) \in \mathbb{R}^2 \,|\, V_n(x,y) = E\}, \tag{80}$$

$$\widetilde{\mathcal{Z}}_n(E) = \{(x,y) \in \mathbb{R}^2 \,|\, \widetilde{V}_n(x,y) = E\}, \; n \geq 2. \tag{81}$$

Furthermore, let $y_n^{(max)}$, $y_n^{(min)}$ and $\widetilde{y}_n^{(max)}$, $\widetilde{y}_n^{(min)}$ denote the two intersection points of the y-axes with the ZVC $\mathcal{Z}_n(E)$ and $\widetilde{\mathcal{Z}}_n(E)$, respectively, where $y_n^{(max)} > y_n^{(min)}$, $\widetilde{y}_n^{(max)} > \widetilde{y}_n^{(min)}$ and $E_{2m}^{(esc)} > E_{2m}$ apply, $n \geq 2$, $m \in \mathbb{N}$. Consequently,

$$V_n(0, y_n^{(max)}) = V_n(0, y_n^{(min)}) = \widetilde{V}_n(0, \widetilde{y}_n^{(max)}) = \widetilde{V}_n(0, \widetilde{y}_n^{(min)}) = E \tag{82}$$

applies.

An analogue of Proposition 1 is shown in the following.

Proposition 4. *The three straight lines*

$$y_1 = \frac{x}{\sqrt{3}}, \quad x_1^{(min)} \leq x \leq x_1^{(max)}, \; (\text{resp. } \widetilde{x}_1^{(min)} \leq x \leq \widetilde{x}_1^{(max)} \;), \tag{83}$$

$$y_2 = -\frac{x}{\sqrt{3}}, \quad x_2^{(min)} \leq x \leq x_2^{(max)}, (\text{resp. } \widetilde{x}_2^{(min)} \leq x \leq \widetilde{x}_2^{(max)} \;), \tag{84}$$

$$x = 0, \quad y_n^{(min)} \leq y_3 \leq y_n^{(max)}, \; (\text{resp. } \widetilde{y}_n^{(min)} \leq y_3 \leq \widetilde{y}_n^{(max)} \;) \tag{85}$$

are 1:1 resonance orbits of the Hamiltonians H_n, $\widetilde{H}_n$ for Energy $E > 0$ and $E_{2m}^{(esc)} > E_{2m}$, $n \geq 2$, $m \in \mathbb{N}$., where

$$x_1^{(min)} = -x_2^{(max)} = -\frac{\sqrt{3}}{2} y_n^{(max)}, \quad x_1^{(max)} = -x_2^{(min)} = -\frac{\sqrt{3}}{2} y_n^{(min)}, \tag{86}$$

$$\widetilde{x}_1^{(min)} = -\widetilde{x}_2^{(max)} = -\frac{\sqrt{3}}{2} \widetilde{y}_n^{(max)}, \quad \widetilde{x}_1^{(max)} = -\widetilde{x}_2^{(min)} = -\frac{\sqrt{3}}{2} \widetilde{y}_n^{(min)}. \tag{87}$$

Proof. Since the x-coordinate of the gradients $(\nabla V_n)(0, y)$ (resp. $(\nabla \widetilde{V}_n)(0, y)$) restricted to $x = 0$ are equally to 0, (85) follows. Due to the above property (i), the assertions (83), (84), (86), (87) are implied analogously to the proof of Proposition 1.

In analogy to the notations given in Remark 1 and Proposition 3 let us introduce the following families of trajectories.

Let $\tau_j^{(n)}$ and $\widetilde{\tau}_j^{(n)}$, $j = 1, 2, 3$, denote the three 1:1 resonance orbits of the Hamiltonians H_n and $\widetilde{H}_n$, respectively, which are given in Proposition 4, $n \geq 2$. Furthermore, let $\sigma_j^{(n)}$ and $\widetilde{\sigma}_j^{(n)}$, $j = 1, 2, 3$, denote the 1:1 resonance orbits of the Hamiltonians H_n and $\widetilde{H}_n$, respectively, which correspond to σ_j of the Toda-Hamiltonian. Finally, let $o_i^{(n)}$ and $\widetilde{o}_i^{(n)}$, $i = 1, 2$, denote the 1:1 periodic central orbit H_n and $\widetilde{H}_n$, respectively, which correspond to o_i of the Toda-Hamiltonian.
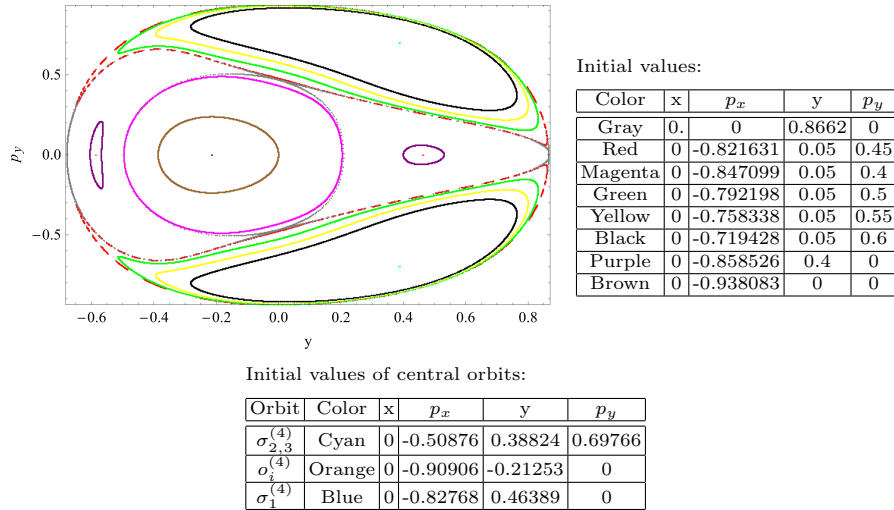
Remark 7. Among the Hamiltonians considered above, there are some such that some of the orbits given above are stable, and others of those orbits are unstable at certain energies.

While the orbits $o_i^{(n)}$, $\widetilde{o}_i^{(n)}$, $i = 1, 2$, are stable for almost all energies $E > 0$, the stability of the orbits $\tau_j^{(n)}$, $\sigma_j^{(n)}$, $\widetilde{\tau}_j^{(n)}$, $\widetilde{\sigma}_j^{(n)}$, $j = 1, 2, 3$, and their bifurcations is very different in dependence on energy E and $n \geq 2$. The stability and non-stability of those orbits will be discussed in the following. Those differences explain e.g. the different properties of the systems H_n, $\widetilde{H}_n$ concerning the existence of separated chaotic seas.

3.2 The fourth order Hamiltonian H_4

As in the case of Toda-Hamiltonian H, approximation of the two central periodic 1:1 orbits o_i given in (60), (61), $i = 1, 2$, are also present in H_4 for each energy $E > 0$. In distinction to the case of Toda-Hamiltonian H, the separatrix $\mathcal{S}(E)$ disappears, and as well stable 1:1 resonance orbits as chaotic areas appear in the Poincaré-section at surface $x = 0$ for energy $E > 0$.

For energies $E < 0.44$ the orbits $\tau_j^{(4)}$, $j = 1, 2, 3$, considered in (83), (84), (85) are unstable. For some energy between $0,44$ and 0.45 they become stable. For $E = 0.45$ they are already stable, see Fig.s 10, 11.

Initial values:

Color	x	p_x	y	p_y
Gray	0.	0	0.8662	0
Red	0	-0.821631	0.05	0.45
Magenta	0	-0.847099	0.05	0.4
Green	0	-0.792198	0.05	0.5
Yellow	0	-0.758338	0.05	0.55
Black	0	-0.719428	0.05	0.6
Purple	0	-0.858526	0.4	0
Brown	0	-0.938083	0	0

Initial values of central orbits:

Orbit	Color	x	p_x	y	p_y
$\sigma_{2,3}^{(4)}$	Cyan	0	-0.50876	0.38824	0.69766
$o_i^{(4)}$	Orange	0	-0.90906	-0.21253	0
$\sigma_1^{(4)}$	Blue	0	-0.82768	0.46389	0

Fig. 10. Poincaré-section of H_4 at surface $x = 0$ with energy $E = 0.44$ for $T = 20000$ time steps. There are three stable 1:1 resonance orbits $\sigma_j^{(4)}$, $j = 1, 2, 3$: the blue and two cyan orbits (because both initial values $p_x = \pm 0.50876$ yield the same Poincaré-section). Furthermore, there are the stable periodic 1:1 orbits o_i, $i = 1, 2$, in orange color. (The initial values of the central orbits are estimated by Nelder-Mead algorithm, see [12], [1, Kap. 2].) Around these stable central orbits there are shown the intersections of several tori with the plane $x = 0$. Of special interest is the region around $y = 0$, $p_y \overset{(34)}{=} \pm \frac{1}{4}\sqrt{8 \cdot 0.44} \approx \pm 0.469$, since there are the intersections of the unstable orbits $\tau_{2,3}^{(4)}$ given in (83), (84) with $x = 0$.
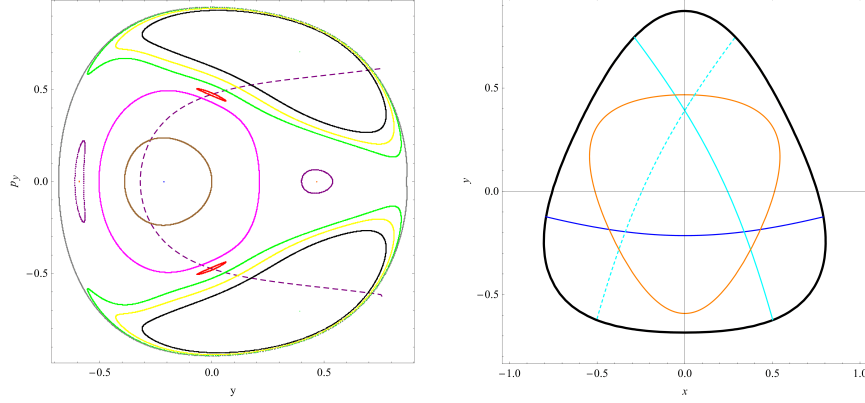
Initial values of central periodic orbits:

Color	x	p_x	y	p_y
Cyan	0	-0.51444	0.391584	0.706067
Cyan - Dashed	0	0.51444	0.391584	0.706067
Blue	0	-0.91945	-0.21433	0.000091937
Orange	0	-0.837687	0.467582	0.000185892

Fig. 11. Poincaré-section of H_4 at surface $x = 0$ for energy $E = 0.45$ and $T = 20000$ time steps. The initial values of the central orbits are given in the above table, and the other initial values of the intersections of the tori with $x = 0$ are the same for x, y, p_y as in Fig. 10, only the initial values of p_x are slightly changed such that $E = 0.45$ holds. The separatrix of the Toda-Hamiltonian for energy $E = 0.45$ is shown as the purple dotted curve. The intersections of the the axes $y = 0$ with the separatrix coincide with the intersections of the orbits (83), (84) with $x = 0$. These orbits are now stable ones since they are attracting, e.g., the red torus is attracted. In the second picture the central periodic 1:1 orbits of type (I) and (II) are shown in the (x, y)-plane, where the colors correspond to those of the Poincaré-section. The black curve represents the ZVC.

For energies $0 < E \leq 1.5$, there are stable, periodic 1:1 orbits $\sigma_j^{(4)}$ in blue color and cyan colors, respectively, see Fig. 11. For energy $E = 1.54$, they disappear, see [22, p. 3398].

For energies $E > 1.5$, the Poincaré sections are dominated by the stable, periodic 1:1 orbits o_i of type (II), $i = 1, 2$, the three stable 1:1 resonance orbits $\tau_j^{(4)}$ of type (I) given in (83), (84), (85), and a chaotic sea, see Fig.s 12, 14. Furthermore, there are periodic orbits of higher order as well of type (I) as of type (II), see Fig.s 13, 15.

The ratio q between the areas of order and stochasticy sensitively depends on E. Since q satisfies

$$\begin{cases} q \approx 1 & \text{for } 0 < E \leq 2 \\ 0.829 \leq q < 1 & \text{for } 2 < E \leq 400 \\ q \approx 1 & \text{for } E > 400 \end{cases} \qquad (88)$$

(see [22, Sec. 2.2.2]), H_4 is not a good candidate for obtaining two separated chaotic regions.
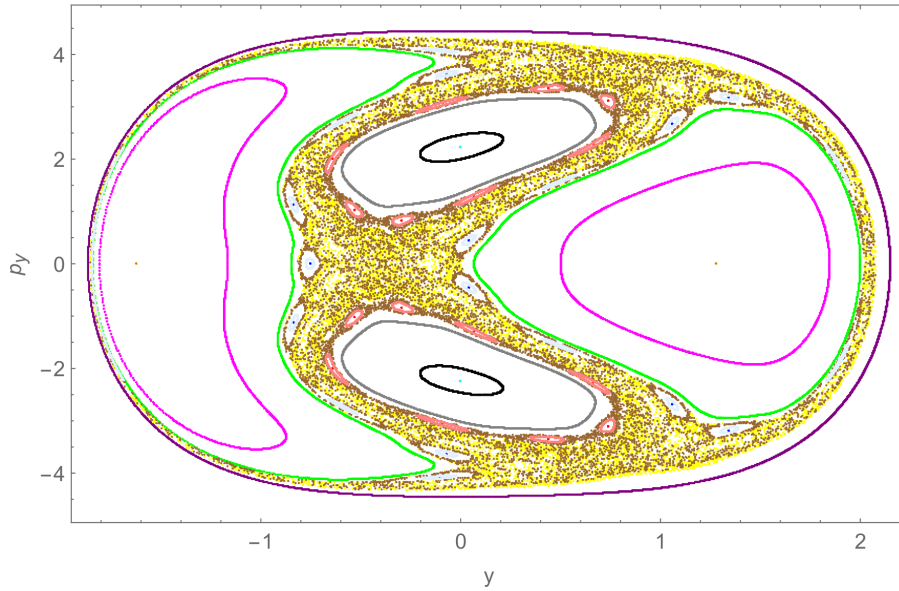
Initial values of central periodic orbits:

Orbit	Color	x	p_x	y	p_y
$\tau_{2,3}^{(4)}$	Cyan	0	-3.87301	-0.0000444858	2.23602
$o_i^{(4)}$	Orange	0	-4.13274	1.27945	0.0000535197
$\tau_1^{(4)}$	Purple	0	-0.797231	2.15	0
	Red	0	-3.12381	0.739733	3.10887
	Blue	0	-4.44886	0.0414841	0.453792

Initial values of trajectories:

Color	Magenta	Green	Black	Grey	Pink	Light Blue	Brown	Yellow
x	0	0	0	0	0	0	0	0
p_x	-4.44644	-2.3094	-4	-4.26351	-4.30813	-4.44939	-3.1241	-4.47214
y	.5	2	0	0	0	0.02	0	0
p_y	0	0	2	1.35	1.2	0.45	3.2	0

Fig. 12. Poincaré-section of H_4 at surface $x = 0$ with energy $E = 10$ for $T = 20000$ time steps. There is as well a big chaotic sea shown in yellow and brown colors as two big regular domains around the central periodic orbits shown in cyan and orange colors, respectively, and also a small regular domain close to the limiting curve shown in purple color. The central periodic 1:1 orbits shown in Fig. 11 in blue and cyan colors, respectively, disappeared now at $E = 10$. There are two stable central periodic 1:1 orbits of type (II) (moving clockwise and anti-clockwise, respectively) shown in orange. Intersection of the plane $x = 0$ with two tori surrounding the orange central orbits are shown in magenta and green colors, respectively. Further, two (moving clockwise and anti-clockwise, respectively) central periodic orbits of period 10 and also of type (II) are shown in blue, and also a torus surrounding the blue central orbits is shown in light blue color. Furthermore, the stable central 1:1 resonance orbits given in (83), (84), (85) are shown in cyan and purple, respectively. Intersection of tori surrounding the orbits in cyan are shown in black and gray, respectively. Moreover, there is a stable central periodic orbit of period 8 and of type (I) shown by a red dot, and this orbit is surrounded by a pink torus. The projections of those periodic orbits into the (x, y)-plane are shown in Fig. 13.
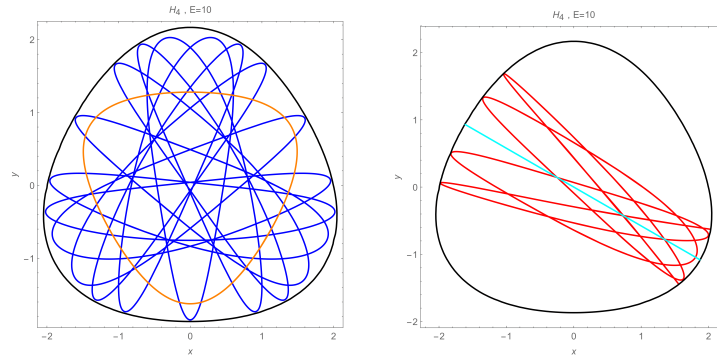
Fig. 13. In the left-hand picture there are shown the important stable, central 1:1 orbits of type (II) in orange color and the stable, periodic orbit of type (II) in blue color for energy $E = 10$. In the right-hand picture the important stable orbit given in (84) is shown in cyan, and a second stable periodic orbit of type (I) is shown in red color. The ZVC $\mathcal{Z}_4(10)$ are given by the black curves. For the initial values of the above orbits, we refer to Fig. 12.
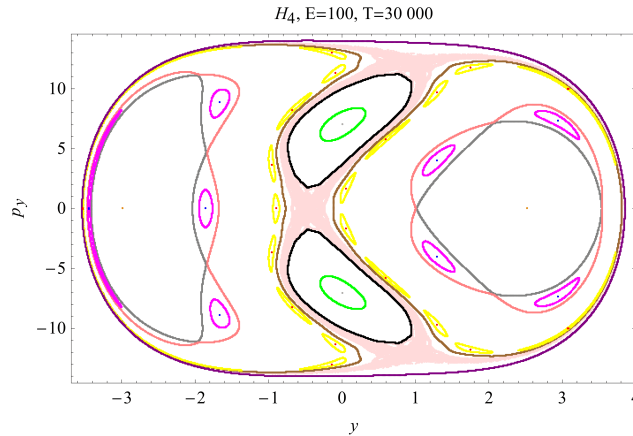

Initial values of central periodic orbits:

Orbit	Color	x	p_x	y	p_y
$\tau_{2,3}^{(4)}$	Cyan	0	± 12.2473	0	7.0713
$\tau_1^{(4)}$	Purple	0	-2	0	14
$o_i^{(4)}$	Orange	0	-12.8057	2.5201	0
	Blue	0	-13.4345	1.29616	4.0574
	Red	0	-14.0439	0.05491	1.6634

Initial values of trajectories:

Color	x	p_x	y	p_y
Green	0	-12.8062	0	6
Black	0	-10	0	10
Brown	0	-8.88819	0	11
Pink	0	$-2\sqrt{149/3}$	1	0
Gray	0	-14.092	1.02	0
Yellow	0	$-2\sqrt{14}$	0	12
Light Red	0	-5.54715	0.5	13

Fig. 14. Poincaré-section of H_4 at surface $x = 0$ for $T = 30000$ time steps and energy $E = 100$. There are the stable, periodic orbits $\tau_{2,3}^{(4)}$, $\tau_1^{(4)}$ and $o_i^{(4)}$, $i = 1, 2$, surrounded by some KAM-tori, which are visible in cyan, purple and orange colors, respectively. Further there are central periodic orbits surrounded by KAM-island of second order, shown in blue and red colors, respectively. For the projections of those orbits into the (x, y)-plane, see Fig. 15. There is also one chaotic sea in light red colors. The topology of that Poincaré-section is very similar to that for $E = 10$, see Fig. 12.
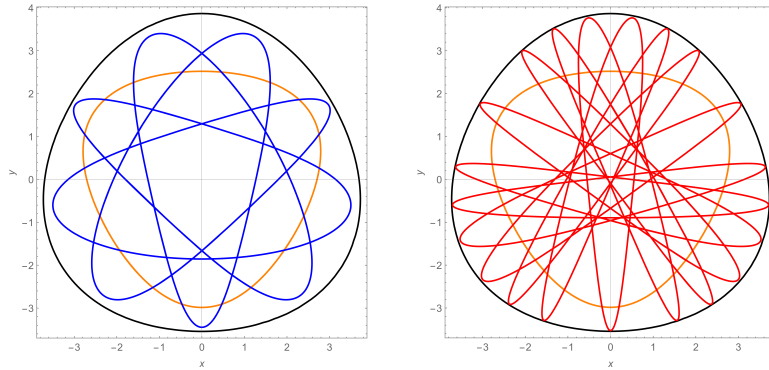
**Fig. 15.** Six periodic orbits of type (II) are shown for H_4 and energy $E = 100$. There are the orbits o_i in orange color, $i = 1, 2$. Further, the two periodic orbits of period 4 (moving clockwise and anti-clockwise, respectively) are shown in blue color in the left-hand picture. In the right-hand picture, the two periodic orbits of type (II) are shown in red color. The ZVC $\mathcal{Z}_4(100)$ are shown in black color. For the initial values of those orbits see Fig. 14.

3.3 The sixth order Hamiltonian H_6

Bifurcations of trajectories $\sigma_j^{(6)}$, $j = 1, 2, 3$. The most interesting feature of H_6 are the trajectories $\sigma_j^{(6)}$ and their bifurcations $\sigma_{j,i}^{(6)}$, $j = 1, 2, 3$, $i = 1, 2$. There is some energy $4.3 < E_0 < 4.4$ such that $\sigma_j^{(6)}$ are stable for energies $E < E_0$, and unstable for energies $E > E_0$. The trajectories $\sigma_j^{(6)}$ bifurcate at energy E_0, and two stable periodic orbits $\sigma_{j,i}^{(6)}$ (moving clockwise and anti-clockwise, respectively) of type (II) appear, see Fig.s 16, 17.
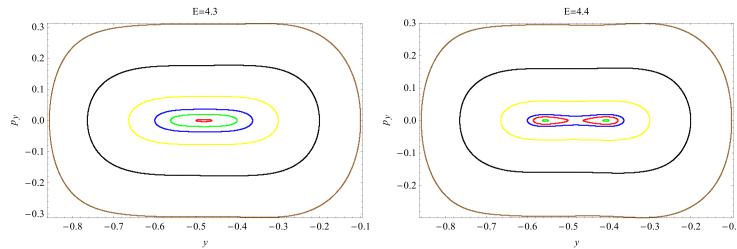
Fig. 16. Bifurcation of $\sigma_1^{(6)}$ for energies between 4.3 and 4.4. Parts of the Poincaré-section of H_6 at surface $x = 0$ for energies $E = 4.3$ and $E = 4.4$, respectively. The bifurcation of $\sigma_1^{(6)}$ is visible, since there is one central orbit within the red torus for $E = 4.3$, and for energy $E = 4.4$ there are two central orbits $\sigma_{1,1}^{(6)}$, $\sigma_{1,2}^{(6)}$ of type (II) (moving clockwise and anti-clockwise, respectively) that are surrounded by the green and red tori. See also Fig. 18 for projections of $\sigma_{1,1}^{(6)}$ into the (x, y)-plane.
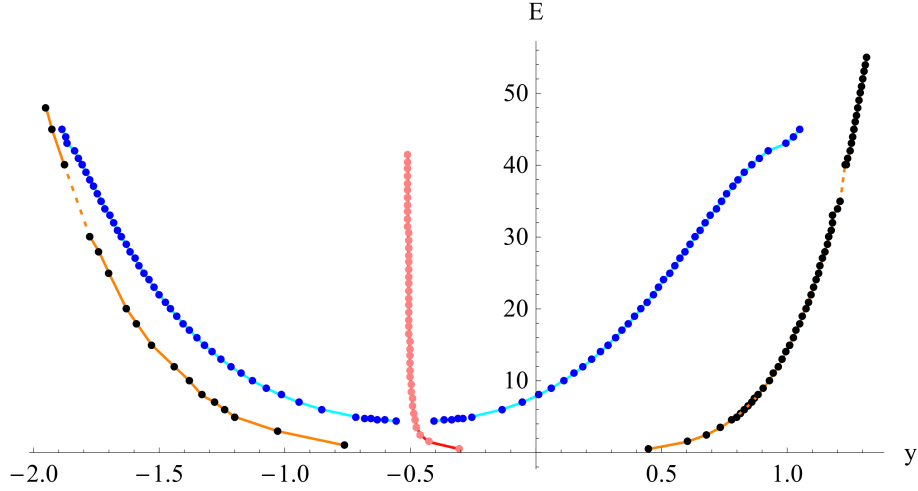
Fig. 17. Bifurcation diagram of H_6 for $\sigma_1^{(6)}$ in red color, where the estimated exact values are given by pink dots. For some energy $4.3 < E < 4.4$, the orbit $\sigma_1^{(6)}$ becomes unstable and two stable orbits $\sigma_{1,i}^{(6)}$, $i = 1, 2$, of type (II) (moving clockwise and anti-clockwise, respectively) appear. The bifurcated orbits $\sigma_{1,i}^{(6)}$ are shown in cyan color, where the exactly estimated values are given by blue dots. The important orbits $o_i^{(6)}$, $i = 1, 2$, are shown in orange color, and the estimated exact values are given by black dots.
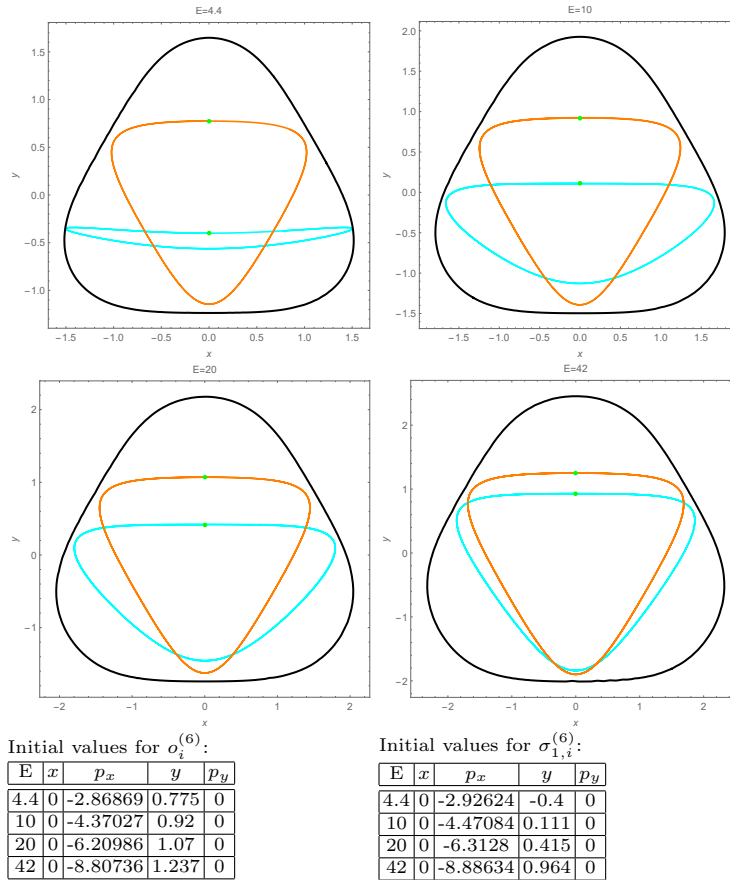
Now the stable, periodic orbits $o_i^{(6)}$ attract those orbits $\sigma_{j,i}^{(6)}$ with increasing energies, see the bifurcation diagram in Fig. 17. Projections of those orbits into the (x, y)-plane are given in Fig. 18. For energies E between 35 and 40, the still stable, orbits $\sigma_{j,i}^{(6)}$ are completely surrounded by KAM-tori of $o_i^{(6)}$, see the Poincaré-section given in Fig. 28. At energy E=43, the orbits $\sigma_{j,i}^{(6)}$ disappeared. The interval $15.2 \leq E \leq 16.4$ of energies is of special interest concerning the existence of two nearly separated chaotic domains, and will be considered in the following.

On the existence of two (nearly) separated chaotic domains.   As explained in Section 1, it is of special interest to find separated chaotic seas. The stable, 1:1 periodic orbits $o_i^{(6)}$, $\sigma_{j,i}^{(6)}$, $(i = 1, 2; j = 1, 2, 3)$, play a crucial role for the appearance of two nearly separated chaotic seas. While the orbits $o_i^{(6)}$ are stable for all energies E beside a small interval $35 < E < 39$, the bifurcated orbits $\sigma_{j,i}^{(6)}$ were attracted with increasing energies, and then completely absorbed by $o_i^{(6)}$ at energy $E \approx 43$, see the bifurcation diagram in Fig. 17.

However, when the orbits $o_i^{(6)}$, $\sigma_{j,i}^{(6)}$ are close enough to each other, the resonance zones associated with neighboring orbits $\sigma_{j,i}^{(6)}$ squeeze holes in some KAM tori of $o_i^{(6)}$. The continuous barrier of such a KAM torus is now transformed to a barrier that is a Cantor set, and called cantorus, see Fig. 24. For phase space
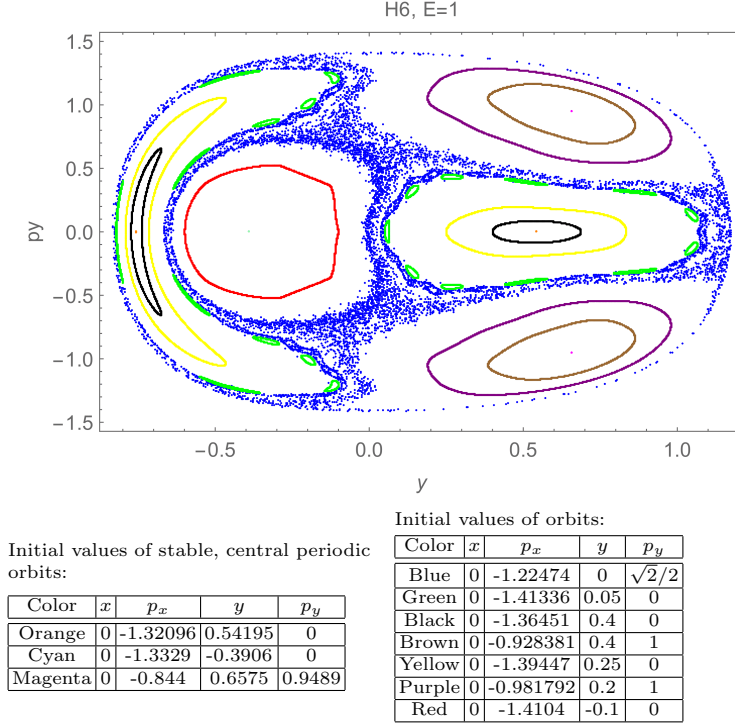
trajectories, it is now possible to pass through cantori after several attempts, since cantori act as turnstiles that allow a two-way flow of traffic. However, cantori can still form a partial barrier, and the leakage is very slow, and such two nearly separated, chaotic seas occur, see [13, ch. 3.9].

Initial values for $o_i^{(6)}$:

E	x	p_x	y	p_y
4.4	0	-2.86869	0.775	0
10	0	-4.37027	0.92	0
20	0	-6.20986	1.07	0
42	0	-8.80736	1.237	0

Initial values for $\sigma_{1,i}^{(6)}$:

E	x	p_x	y	p_y
4.4	0	-2.92624	-0.4	0
10	0	-4.47084	0.111	0
20	0	-6.3128	0.415	0
42	0	-8.88634	0.964	0

Fig. 18. Projections of $\sigma_{1,i}^{(6)}$ in cyan and $o_i^{(6)}$ in orange color, $i = 1, 2$, are shown for several energies between 4.4 and 42. The green dots indicate the initial values of the trajectories which are given in the above table. The ZVC are represented by the black curves. The above pictures show how the orange orbits $o_i^{(6)}$ attract the cyan orbits $\sigma_{1,i}^{(6)}$ with increasing energy. See also the bifurcation diagram given in Fig. 17

The existence of such nearly separated chaotic seas depends very sensitive on the energy E of the system. Along these lines, we considered randomly chosen trajectories with initial values inside one chaotic sea and estimated the empirical probability h for entering the other chaotic sea after $T = 30000$ time steps. We got the best values with $6.6\% < h < 55\%$ for energies $15.2 < E < 16.4$, see Fig. 23. For other energies, h is significantly higher.

At energy $E = 35$ there are two completely separated chaotic seas, see Fig. 27. At that energy some KAM-tori of $o_i^{(6)}$ completely separate those two chaotic seas.

H6, E=1

Initial values of stable, central periodic orbits:

Color	x	p_x	y	p_y
Orange	0	-1.32096	0.54195	0
Cyan	0	-1.3329	-0.3906	0
Magenta	0	-0.844	0.6575	0.9489

Initial values of orbits:

Color	x	p_x	y	p_y
Blue	0	-1.22474	0	$\sqrt{2}/2$
Green	0	-1.41336	0.05	0
Black	0	-1.36451	0.4	0
Brown	0	-0.928381	0.4	1
Yellow	0	-1.39447	0.25	0
Purple	0	-0.981792	0.2	1
Red	0	-1.4104	-0.1	0

Fig. 19. Poincaré - section of H_6 at surface $x = 0$ for energy $E = 1$ and T=20000 time steps. There are visible the stable, periodic central orbits $o_i^{(6)}$, $\sigma_1^{(6)}$ and $\sigma_{2,3}^{(6)}$ given by the dots in orange, cyan and magenta colors, respectively. The orbits $\tau_j^{(6)}$, $j = 1, 2, 3$, are unstable, and the blue dots are the Poincaré - section of $\tau_2^{(6)}$ after T=20000 time steps.

Bifurcations of trajectories $\tau_j^{(6)}$, $j = 1, 2, 3$. The 1:1 periodic, resonance orbits $\tau_j^{(6)}$ are considered in Proposition 4. For energies $E < 1.8$ those orbits $\tau_j^{(6)}$ are unstable, see Fig. 19. For energies $1.4 < E < 5.8$, the orbits $\tau_j^{(6)}$ are stable, see Fig. 20. At energy $E \approx 5.3$, the 4:4 periodic, resonance orbits $\tau_{j,1}^{(6)}$ of type (I) appear. At energy $E \approx 5.8$, $\tau_j^{(6)}$ bifurcate into 2:2 periodic, resonance orbits $\tau_{j,1}^{(6)}$ of type (I), and then $\tau_j^{(6)}$ becomes unstable, see Fig. 21.

For energies $6 \leq E \leq 20$, both families $\tau_{j,1}^{(6)}$ and $\tau_{j,2}^{(6)}$ of periodic orbits are stable, see Fig. 22. While $\tau_{j,2}^{(6)}$ becomes unstable for some energy $21 < E < 23$, $\tau_{j,1}^{(6)}$ is still stable at energy $E = 30$, see Fig.s 25, 26. At energy $E = 40$, $\tau_{j,1}^{(6)}$ is also unstable, see Fig. 28.
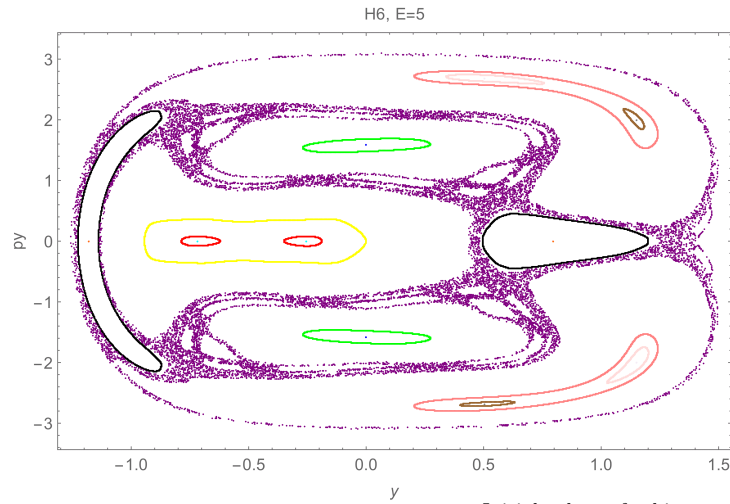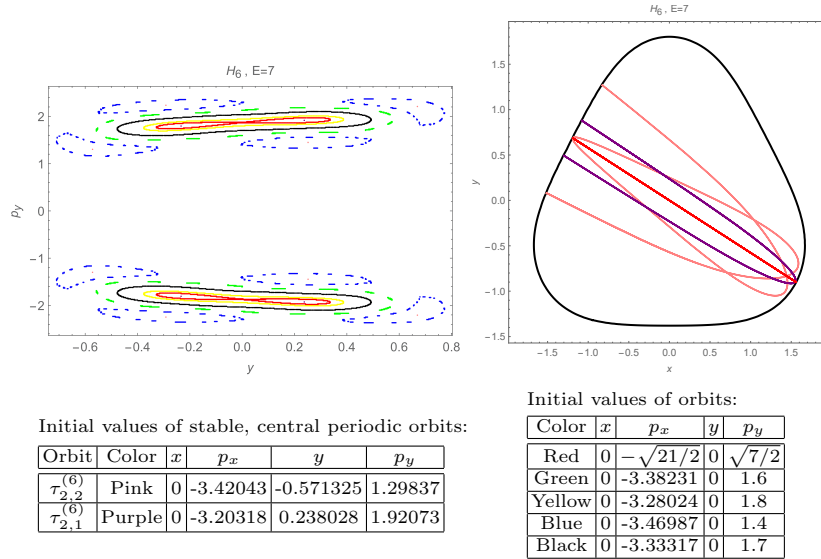
Initial values of stable, central periodic orbits:

Orbit	Color	x	p_x	y	p_y
$o_i^{(6)}$	Orange	0	-3.06392	0.797137	0
$\sigma_{1,i}^{(6)}$	Cyan	0	-3.14941	-0.25504	0
$\sigma_{2,i}^{(6)}$	Light Blue	0	-2.04001	1.14983	-1.99795
$\sigma_{3,i}^{(6)}$	Gray	0	-2.04035	1.14994	1.99746
$\tau_2^{(6)}$	Blue	0	$-\sqrt{15/2}$	0	$\sqrt{5/2}$

Initial values of orbits:

Color	x	p_x	y	p_y
Green	0	-2.78147	0.12	1.5
Brown	0	-2.13131	1.15	1.9
Yellow	0	$-\sqrt{10}$	0	0
Purple	0	-2.97689	0.4	1
Black	0	-2.79955	1.2	0
Red	0	-3.1352	-0.35	0
Pink	0	-1.42193	0.4	2.8
Light Red	0	-2.14417	1.2	-1.8

Fig. 20. Poincaré-section of H_6 at surface $x = 0$ for energy $E = 5$ and $T = 20000$ time steps. There are the central, periodic orbits $o_i^{(6)}$, $\sigma_{j,i}^{(6)}$, $i = 1, 2; j = 1, 2, 3$, which are of type (II). Further the stable orbit $\tau_2^{(6)}$ of type (I) is visible. (For the initial values and colors, see the above table.) The stability of those orbits is obvious since each of them are surrounded by quasi-periodic tori shown in black, red, green light red and brown, respectively. Furthermore, a chaotic sea is visible in purple color.

Initial values of stable, central periodic orbits:

Orbit	Color	x	p_x	y	p_y
$\tau_{2,2}^{(6)}$	Pink	0	-3.42043	-0.571325	1.29837
$\tau_{2,1}^{(6)}$	Purple	0	-3.20318	0.238028	1.92073

Initial values of orbits:

Color	x	p_x	y	p_y
Red	0	$-\sqrt{21/2}$	0	$\sqrt{7/2}$
Green	0	-3.38231	0	1.6
Yellow	0	-3.28024	0	1.8
Blue	0	-3.46987	0	1.4
Black	0	-3.33317	0	1.7

Fig. 21. Bifurcation of $\tau_2^{(6)}$. At the figure on the left-hand side, a part of the Poincaré-section of H_6 at surface $x = 0$ for energy $E = 7$ and $T = 20000$ time steps is shown. While the trajectory $\tau_2^{(6)}$ shown in red color became unstable, the trajectories $\tau_{2,1}^{(6)}$ and $\tau_{2,2}^{(6)}$ shown in purple and pink, respectively, are stable. At the figure on the right-hand side, the projection of the unstable orbit $\tau_2^{(6)}$ into the (x, y)-plane is shown in red. Furthermore, the stable, periodic orbits $\tau_{2,1}^{(6)}$ and $\tau_{2,2}^{(6)}$ of type (I) are shown in purple and pink, respectively.
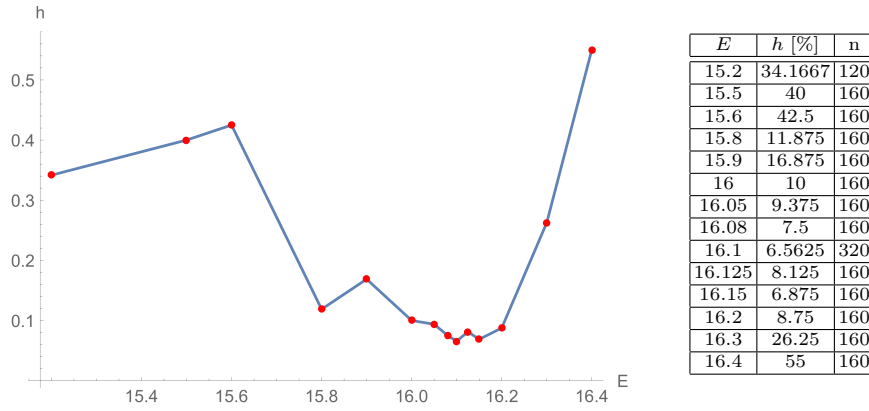
H_6, E=16.1

Initial values of orbits and chaotic seas:

Color	x	p_x	y	p_y
Blue	0	-5.65128	0.55	0
Red	0	-5.48064	1.2	0
Green	0	-4.91245	1.4	2
Yellow	0	-4.91245	1.4	-2
Purple	0	-5.41664	-0.32	1.65
Brown	0	-5.07265	-0.6	2.4
Pink	0	-3.62597	1.9	0.7
Black	0	-1.76666	2.05	0.9
Light Red	0	-5.31037	0	2
Light Blue	0	-5.40685	1.3	0
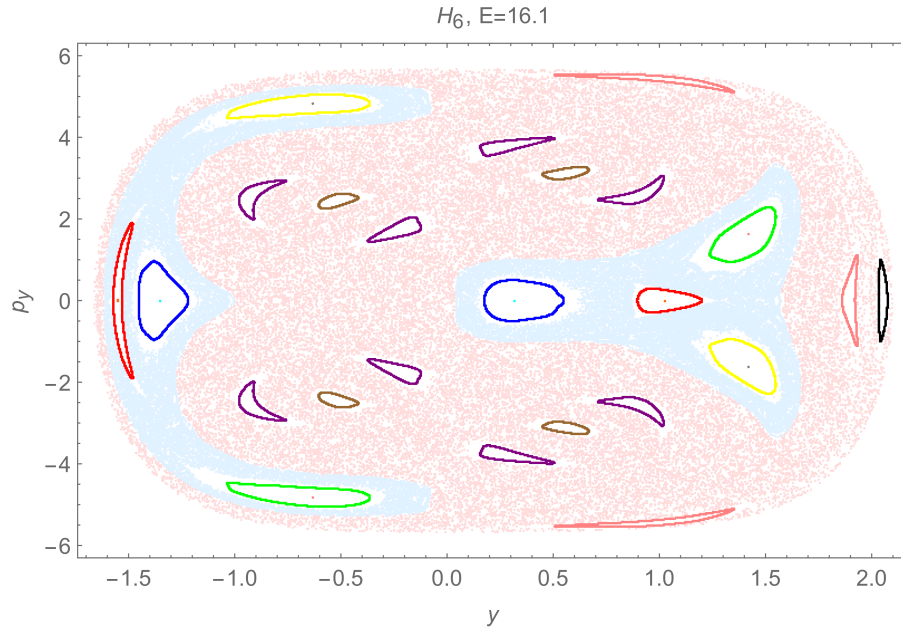
Initial values of stable, central periodic orbits of type (II):

Orbit	Color	x	p_x	y	p_y
$o_i^{(6)}$	Orange	0	-5.56324	1.02531	0
$\sigma_{1,i}^{(6)}$	Cyan	0	-5.66671	0.318219	0
$\sigma_{2,i}^{(6)}$	Gray	0	-5.02175	1.42194	-1.61957
$\sigma_{3,i}^{(6)}$	Magenta	0	-5.02175	1.42194	1.61957

Fig. 22. Poincaré-section of H_6 at surface $x = 0$ for energy $E = 16.1$ and $T = 40000$ time steps. The trajectories in light red and light blue colors fill two big chaotic seas which are completely separated. Inside the chaotic see in light blue, there are the stable, 1:1 periodic orbits $o_i^{(6)}, \sigma_{j;i}^{(6)}$, $i = 1, 2$; $j = 1, 2, 3$. Those orbits are surrounded by the blue, red, green and yellow tori, respectively. Inside the chaotic sea in light red, there are visible the intersections of the brown, purple, black and pink tori with the plane $x = 0$, where the central periodic orbits are $\tau_{2,1}^{(6)}, \tau_{2,2}^{(6)}$, $\tau_{1,1}^{(6)}$ and $\tau_{1,2}^{(6)}$, respectively, and not shown. (The orbits $\tau_{2,1}^{(6)}, \tau_{2,2}^{(6)}$ and $\tau_{3,1}^{(6)}, \tau_{3,2}^{(6)}$ coincide in the Poincaré-section.)

E	h [%]	n
15.2	34.1667	120
15.5	40	160
15.6	42.5	160
15.8	11.875	160
15.9	16.875	160
16	10	160
16.05	9.375	160
16.08	7.5	160
16.1	6.5625	320
16.125	8.125	160
16.15	6.875	160
16.2	8.75	160
16.3	26.25	160
16.4	55	160

Fig. 23. Empirical probability h for leaving the chaotic sea after $T = 30000$ time steps in dependence on energy E. We considered $n = 160$ and $n = 320$ trajectories, respectively, which are randomly chosen from the rectangle $0.7 < y < 0.8$, $-0.7 < p_y < 0.7$ and counted the number r of trajectories which leave the chaotic domain shown in light blue color in Fig. 22 after $T = 30000$ time steps. The estimated empirical probabilities $h = \frac{r}{n}$ in dependence on E are shown above. Best values are achieved for $15.8 \leq E \leq 16.2$.

H_6, E=16.2
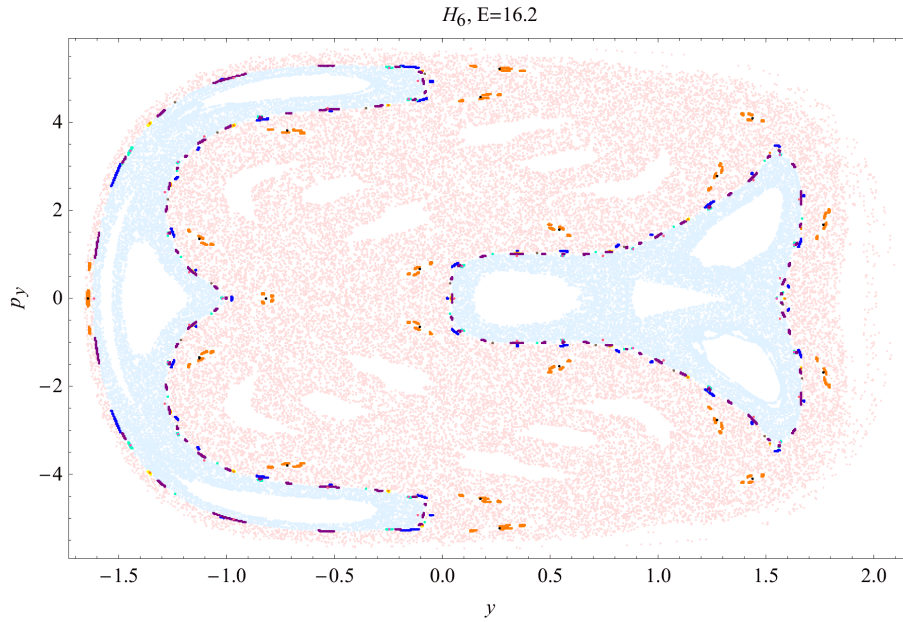
Initial values of periodic orbits of type (II) and cantori:

Color	x	p_x	y	p_y
Orange	0	-1.29847	-1.645	0
Black	0	-1.43731	-1.64057	0.000345736
Blue	0	-5.69204	0.0254917	$-1.17125 \cdot 10^{-6}$
Yellow	0	-5.01483	1.585	0
Red	0	-5.01248	1.58605	-0.0000132236
Cyan	0	-5.08851	1.55	0
Magenta	0	-5.08609	1.55122	0.0000260892
Green	0	-5.02248	1.5807	0.137106
Brown	0	-5.02248	1.5807	-0.137106
Purple	0	-1.9774	-1.60058	1.1865
Pink	0	-2.04652	-1.61492	-0.00048123

Initial values of chaotic seas:

Color	x	p_x	y	p_y
Light Red	0	-5.32917	0	2
Light Blue	0	-5.64567	0.75	0

Fig. 24. Poincaré-section of H_6 at surface $x = 0$ for energy $E = 16.2$ and $T = 30000$ time steps. The border between the two chaotic seas visible in light red and light blue colors is filled with periodic orbits and cantori.
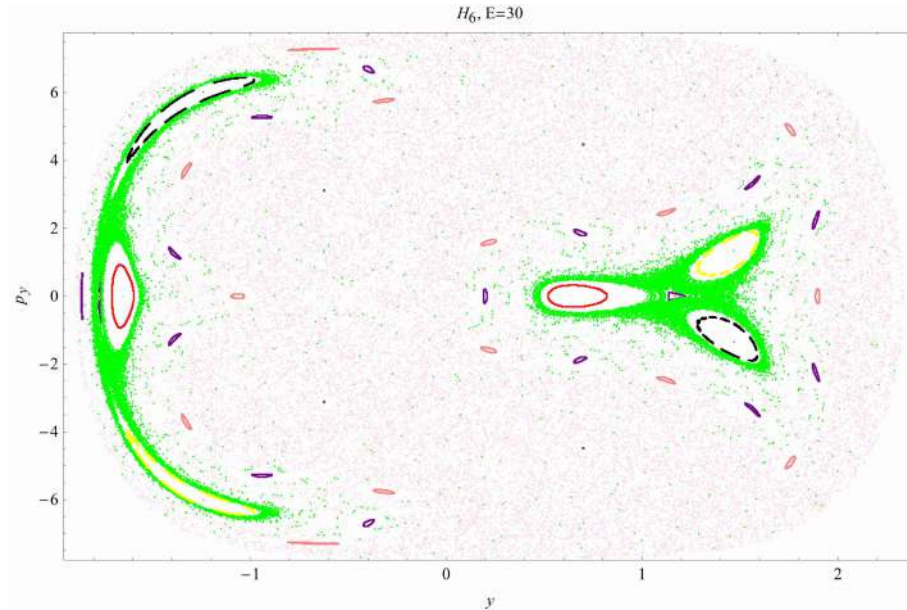
Initial values of stable, central periodic orbits:

Orbit	Color	x	p_x	y	p_y
$o_i^{(6)}$	Orange	0	-7.61964	1.16569	0
$\sigma_{1,i}^{(6)}$	Cyan	0	-7.72286	0.634328	0
$\sigma_{2,i}^{(6)}$	Gray	0	-7.28889	1.46846	-1.35158
$\sigma_{3,i}^{(6)}$	Magenta	0	-7.28889	1.46846	1.35158
$\tau_{2,1}^{(6)}$	Brown	0	-6.28353	0.7	4.48

Initial values of orbits:

Color	x	p_x	y	p_y
Black	0	-7.48365	1.36	-0.64
Yellow	0	-7.48365	1.36	0.64
Blue	0	-7.63135	1.135	0
Green	0	-7.55209	1.3	0
Red	0	-7.70335	0.82	0
Purple	0	-7.74386	0.19	0
Pink	0	-7.59719	0.19	1.5
Light Red	0	-7.74596	0.01	0.00002

Fig. 25. Poincaré-section of H_6 at surface $x = 0$ for energy $E = 30$ and $T = 20000$ time steps. One big chaotic sea is visible in light red and green colors. There are the stable, 1:1 periodic orbits $o_i^{(6)}$ which attract the the still stable, 1:1 periodic orbits $\sigma_{j,i}^{(6)}$, $i = 1, 2$; $j = 1, 2, 3$. The stability of those orbits is obvious since they are surrounded by the KAM-tori in blue, red, yellow and black, respectively. Further the stable orbit $\tau_{2,1}^{(6)}$ is visible in brown color. Furthermore, there are stable, central, periodic orbits of period $p = 7$ of type (II), which are surrounded by the purple and pink tori, respectively (see also Fig. 26).
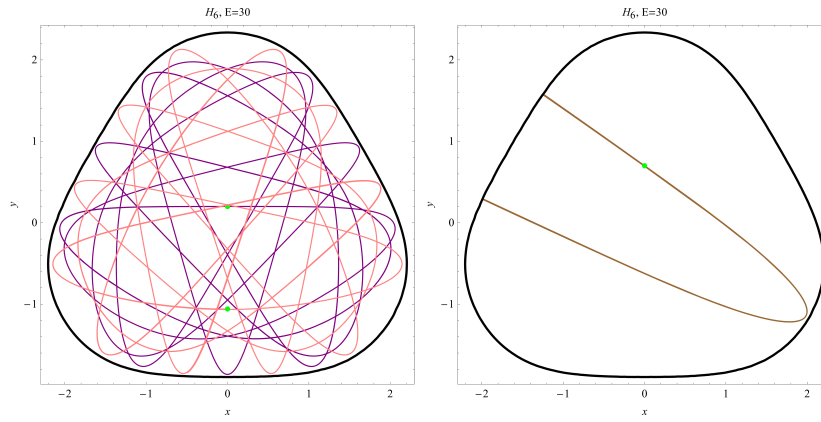
Fig. 26. The projections of the central, periodic orbits of period $p = 7$ described in Fig. 25 into the (x, y)-plane are shown in the left-hand picture, where the color corresponds to the color of the tori visible in Fig. h6-fig8. It is visible that those orbits are of type (II). The projection of the stable central orbit $\tau_{2,1}^{(6)}$ into the (x, y)-plane is shown in brown in the right-hand picture. Furthermore, the ZVC $\mathcal{Z}_6(30)$ are shown by the black curves.

H_6, E=35, T=30 000
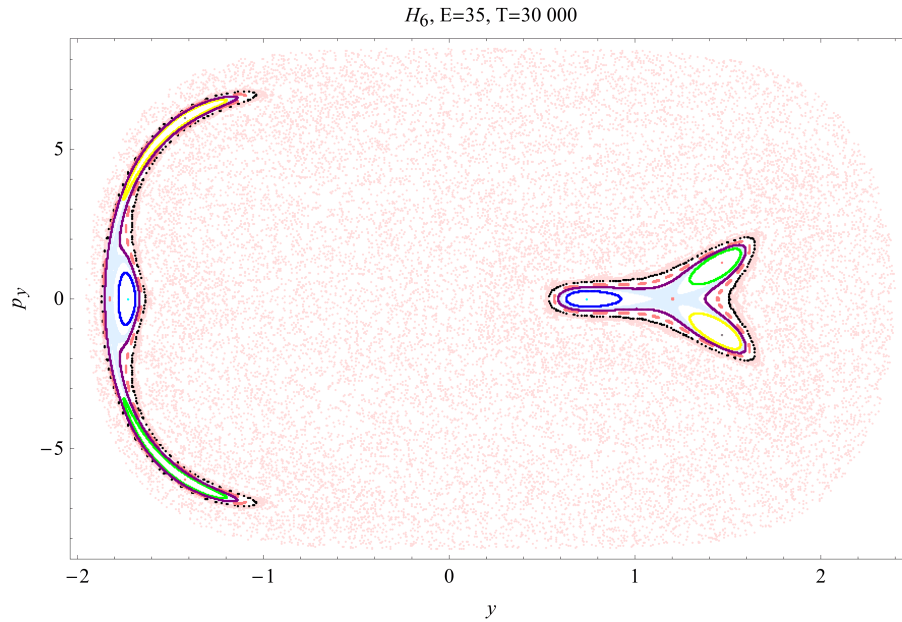
Initial values of central periodic orbits:

Orbit	Color	x	p_x	y	p_y
$o_i^{(6)}$	Orange	0	-8.23635	1.2	0
$\sigma_{1,i}^{(6)}$	Cyan	0	-8.33629	0.737905	0
$\sigma_{2,i}^{(6)}$	Magenta	0	-7.97165	1.4656	1.20526
$\sigma_{3,i}^{(6)}$	Gray	0	-7.97165	1.4656	-1.20526

Initial values of orbits:

Color	x	p_x	y	p_y
Purple	0	-8.21447	1.2	0.6
Pink	0	-8.07705	1.45	0
Black	0	-8.0159	1.51	0
Blue	0	-8.34553	0.63	0
Green	0	-8.16826	1.3	0.56
Yellow	0	-8.16826	1.3	-0.56

Initial values of chaotic seas:

Color	x	p_x	y	p_y
Light Red	0	-7.99282	1.53	0
Light Blue	0	-7.98318	1.41	1.439

Fig. 27. Poincaré-section of H_6 at surface $x = 0$ for energy $E = 35$ and $T = 30000$ time steps. There are visible two completely separated chaotic seas, a big one and a small one in light red and light blue, respectively. The stable, central orbits $\sigma_{j,i}^{(6)}$, j=1,2,3, are surrounded by their KAM tori in blue, green and yellow colors, respectively. There is also visible a KAM torus of $o_i^{(6)}$ in purple. That KAM torus prevents the chaotic sea of light blue color to communicate with the chaotic sea in light red color. Furthermore, a quasi periodic orbit and a cantorus are visible in pink and black colors, respectively.
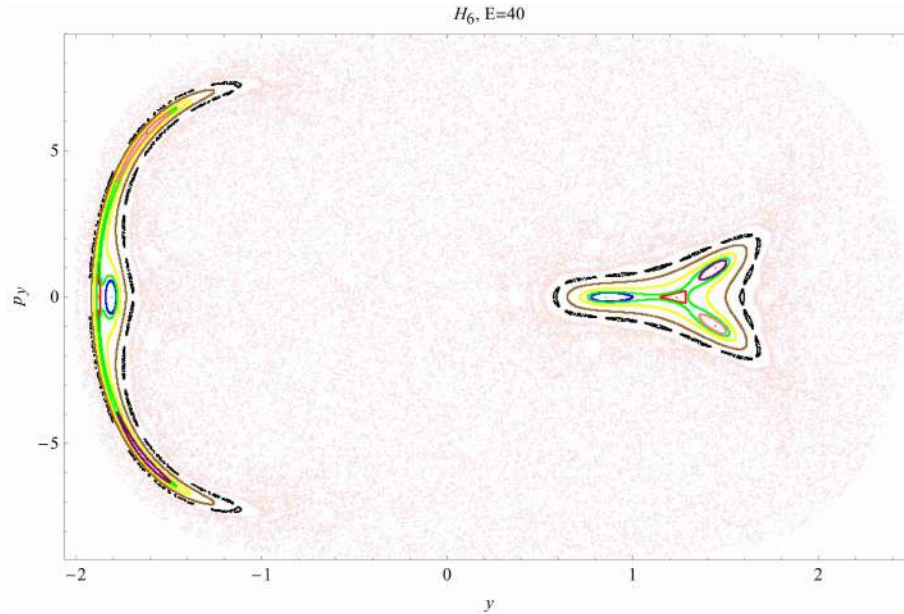
Initial values of stable, central periodic orbits:

Orbit	Color	x	p_x	y	p_y
$o_i^{(6)}$	Orange	0	-8.80762	1.23641	0
$\sigma_{1,i}^{(6)}$	Cyan	0	-8.90283	0.856947	0
$\sigma_{2,i}^{(6)}$	Magenta	0	-8.62061	1.44639	0.988712
$\sigma_{3,i}^{(6)}$	Gray	0	-8.62061	1.44639	-0.988712

Initial values of orbits:

Color	x	p_x	y	p_y
Light Red	0	-8.94427	0.01	0.000021
Purple	0	-8.71809	1.36	0.64
Blue	0	-8.87944	1	0
Green	0	-8.77691	1.3	0
Black	0	-8.50914	1.6	0
Pink	0	-8.71809	1.36	-0.64
Red	0	-8.84039	1.15	0
Brown	0	-8.62735	1.5	0
Yellow	0	-8.7139	1.4	0

Fig. 28. Poincaré-section of H_6 at surface $x = 0$ for energy $E = 40$ and $T = 20000$ time steps. The central, 1:1 periodic obits $o_i^{(6)}$ and $\sigma_{j,i}^{(6)}$, $i = 1, 2$; $j = 1, 2, 3$ are stable since they are surrounded by their KAM-tori in red, pink, magenta and blue color respectively. But the orbits $\sigma_{j,i}^{(6)}$ are already surrounded by the green, yellow and brown KAM-tori of $o_i^{(6)}$. This indicates that $\sigma_{j,i}^{(6)}$ will be absorbed by $o_i^{(6)}$. Further there is one big chaotic sea visible in light red color, and the orbits $\tau_{2,i}^{(6)}$ disappeared.

3.4   The difference Hamiltonian $\widetilde{H}_2$

For low energy $E \approx 1$, a big chaotic sea dominates the Poincaré-section at surface $x = 0$, and the periodic orbits $\widetilde{o}_i^{(2)}$, $i = 1, 2$, are stable since they are surrounded by KAM-tori, see Fig. 29.
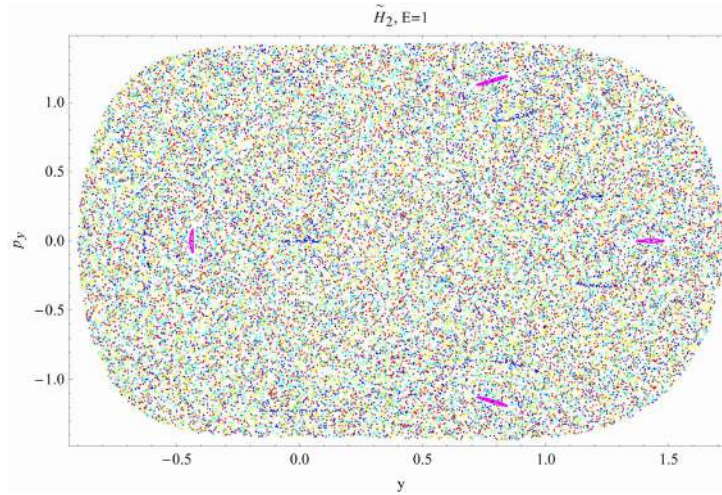
Initial values of central orbits $\widetilde{o}_i^{(2)}$,
$i = 1, 2$:

Color	x	p_x	y	p_y
Black	0	$\pm$ 1.17934	1.42781	0

Initial values of orbits:

Color	x	p_x	y	p_y
Magenta	0	-1.24314	1.37	0
Blue	0	-1.30215	1.3	0
Red	0	-0.834017	1.3	1
Cyan	0	-1.35016	-0.5	0
Yellow	0	-1.42677	0.5	0

Fig. 29. Poincaré-section of $\widetilde{H}_2$ at surface $x = 0$ for energy $E = 1$ and $T = 20000$ time-steps. There is a very big chaotic sea and a small regular region with the magenta KAM torus which surrounds the stable, periodic 2:2 central orbits $\widetilde{o}_i^{(2)}$, $i = 1, 2$, shown in black color, see also Fig. 30.
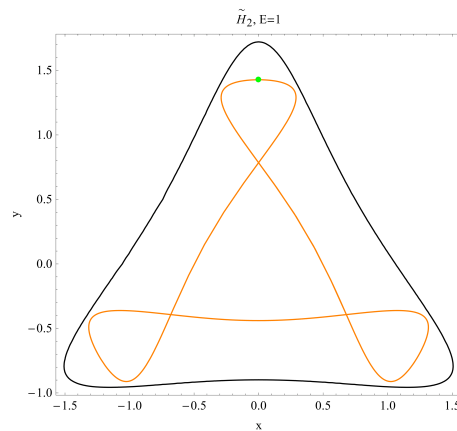
Fig. 30. Periodic 2:2 orbits $\widetilde{o}_i^{(2)}$, $i = 1, 2$, of $\widetilde{H}_2$ at energy $E = 1$ in orange color. The green dot indicates the initial values $x = 0, p_x = \pm 1.17934, y = 1.42781, p_y = 0$ of the trajectories. The ZVC is shown in black color.

Energy $E = 12$ is most interesting for $\widetilde{H}_2$ since there are three completely separated chaotic seas, see Fig. 31. A big chaotic sea visible in light blue color surrounds as well the orbits $\widetilde{o}_i^{(2)}$, $i = 1, 2$, in orange as the periodic orbits in cyan. Inside a second chaotic sea in light red color, there are the stable periodic orbits $\widetilde{\tau}_j^{(2)}$, $j = 1, 2, 3$, surrounded by KAM-tori. That chaotic sea is located around the separatrix $\mathcal{S}(12)$ of Toda-Hamiltonian, see (34). Furthermore, a third chaotic sea is visible in green color, and it is located around the stable, periodic orbit $\tilde{\sigma}_1^{(2)}$ of type (II) visible in blue color, see Fig.s 31,32.

Finally, $\widetilde{H}_2$ becomes nearly regular for high energies ($E = 200$), and the Poincaré-sections of $\widetilde{H}_2$ and the Toda-Hamiltonian are similar, see Fig.s 3, 33. The main difference between those systems is the periodicity of the central orbits o_i and $\widetilde{o}_i^{(2)}$, $i = 1, 2$. While o_i are periodic 1:1, the orbits $\widetilde{o}_i^{(2)}$ are periodic 2:2, see Fig. 30.

A detailed investigation of $\widetilde{H}_n$, $n \geq 2$, will be given in a forthcoming paper.

4   Conclusion

The main feature of the Toda-Hamiltonian are the stable, central 1:1 periodic orbits o_i, $i = 1, 2$, of type (II) and the separatrix $\mathcal{S}(E)$, where each point of $\mathcal{S}(E)$ corresponds to an unstable periodic 1:1 resonance orbit of type (I), see Fig. 4.

Considering the approximants H_4, H_6, $\widetilde{H}_2$ we observe that on one hand the corresponding orbits $o_i^{(4)}$, $o_i^{(6)}$, $\widetilde{o}_i^{(2)}$ are present and stable for almost all energies but on the other hand the separatrix $\mathcal{S}(E)$ disappears. Instead of $\mathcal{S}(E)$, chaotic sea(s) and two families $\tau_j^{(4)}$, $\sigma_j^{(4)}$ and $\tau_j^{(6)}$, $\sigma_j^{6)}$, $j = 1, 2, 3$, of central periodic orbits appear for H_4 and H_6, respectively. The differences between those orbits explain the different behavior of H_4 and H_6.

While $\tau_j^{(4)}$ are stable for all energies $E > 0.45$, the central periodic orbits $\tau_j^{(6)}$ become unstable and they bifurcate into $\tau_{j,1}^{(6)}$ at energy $E \approx 5.8$, $j = 1, 2, 3$. All of those orbits are of type (I). The stability of $\tau_j^{(4)}$ is the reason for that H_4 is nearly regular for high energies, see (88). On the other hand, the instability of $\tau_j^{(6)}$ is the reason for that there is a big chaotic sea such that the ratio q between the areas of order and stochasticity satisfies $q \approx \frac{1}{3}$ for high energies, see [22, Fig. 8].

The different behavior of $\sigma_j^{(4)}$ and $\sigma_j^{(6)}$ is most interesting, since it explains the existence of as well two nearly separated chaotic seas for energies $16 \leq E \leq 16.2$ as two completely separated chaotic seas at $E = 35$ for H_6. While $\sigma_j^{(4)}$ disappear for $E \geq 1.54$, $\sigma_j^{(6)}$ bifurcate at $E \approx 4.3$, and two periodic 1:1 orbits $\sigma_{j,i}^{(6)}$ ($i = 1, 2$, moving clockwise and anti-clockwise, respectively) of type (II) are created by $\sigma_j^{(6)}$, which are of type (I), $j = 1, 2, 3$. Now, $\sigma_{j,i}^{(6)}$ are attracted by $o_i^{(6)}$ for energies $4.3 < E < 43$, and they disappear for $E \geq 43$. This phenomenon explains the existence of respectively, two nearly and two completely separated chaotic seas for H_6.

Finally, the Hamiltonian $\widetilde{H}_2$ is most interesting since there are three completely separated chaotic seas for energy $E = 12$.

$$\widetilde{H}_2,\ E=12$$
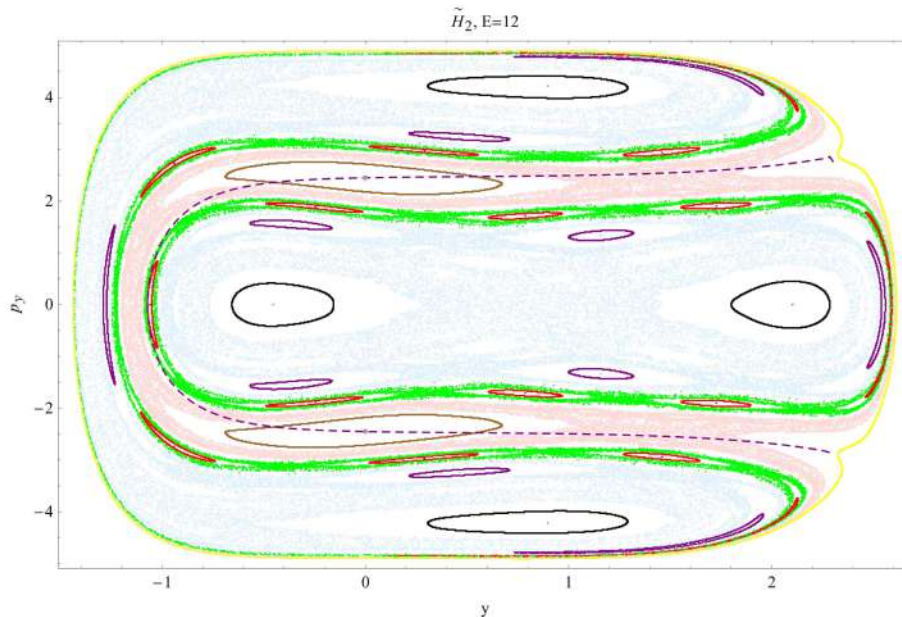
Initial values of stable, central periodic orbits:

Orbit	Color	x	p_x	y	p_y
$\tilde{o}_i^{(2)}$	Orange	0	-4.18478	2.10184	0
$\tilde{\tau}_{2,3}^{(2)}$	Magenta	0	$-3\sqrt{2}$	0	$\pm\sqrt{6}$
	Cyan	0	-4.70294	1.15765	1.33554
$\tilde{\sigma}_1^{(2)}$	Blue	0	4.28182	1.72584	1.90586

Initial values of orbits:

Color	x	p_x	y	p_y
Purple	0	-4.70294	1.15765	1.33554
Black	0	-4.62496	1.8	0
Yellow	0	-1.80332	2.33	2.97
Brown	0	-4.21731	0.5	2.5
Red	0	-4.63033	0	1.6

Initial values of chaotic seas:

Color	x	p_x	y	p_y
Green	0	-4.59456	0	1.7
Light Red	0	-4.21509	1	2.5
Light Blue	0	-4.90071	1	0

Fig. 31. Poincaré-section of $\widetilde{H}_2$ at surface $x = 0$ for energy $E = 12$ and $T = 40000$ time-steps. There are three chaotic seas in light blue, light red and green colors, respectively. Furthermore, stable, central periodic orbits and some KAM-tori are visible. For more explanation, see Section 3.4.
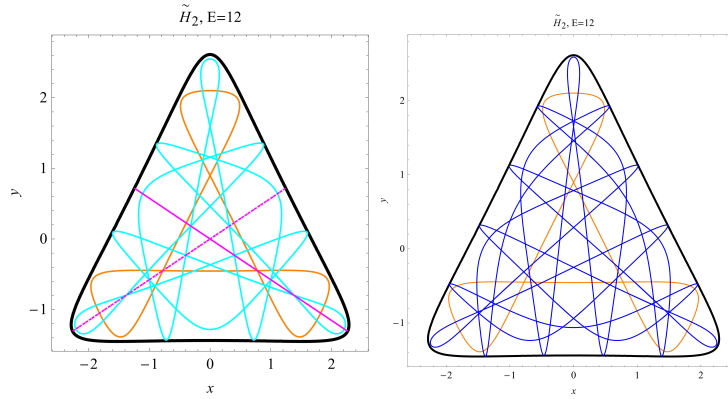
Fig. 32. Projections of the stable, central periodic obits considered in Fig. 31 into the (x, y)-plane. In the left-hand figure there are the periodic 1:1 resonance orbits $\tilde{\tau}_2^{(2)}$ and $\tilde{\tau}_3^{(2)}$ of type (I) in magenta and magenta dashed line, respectively. Furthermore, the 2:2 periodic orbits $\tilde{o}_i^{(2)}$, $i = 1, 2$, of type (II) is shown in orange color. The initial values of the two periodic orbits (moving clockwise and anti-clockwise, respectively) in cyan color are given in Fig. 31. In the right-hand figure the orbits $\tilde{o}_i^{(2)}$, $i = 1, 2$, and the periodic orbits $\tilde{\sigma}_i^{(2)}$ of type (II) are shown in orange and blue color, respectively.

Initial values of orbits:

Color	x	p_x	y	p_y
Blue	0	-17.0841	-1.8	0
Red	0	-19.2061	-1.5	0
Green	0	-19.7876	-1.2	0
Yellow	0	-19.9495	-0.9	0
Black	0	-19.991	-0.6	0
Brown	0	-19.9993	-0.3	0
Purple	0	-20.	0	0
Pink	0	-20.0003	0.3	0
Cyan	0	-20.0012	0.6	0
Orange	0	-20.0012	0.9	0
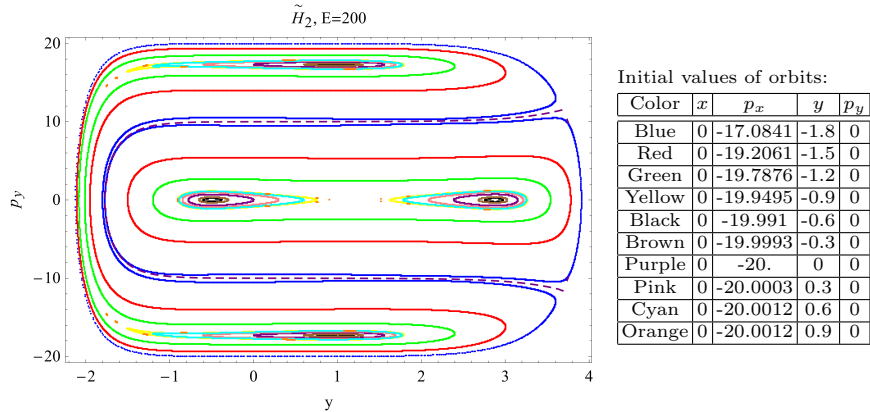
Fig. 33. Poincaré-section of $\widetilde{H}_2$ at surface $x = 0$ for energy $E = 200$ and $T = 20000$ time-steps. The separatrix of the Toda Hamiltonian is shown by the dashed curve in purple color.

Acknowledgments

References

1. W. Alt. *Nichtlineare Optimierung*, Vieweg & Sohn Verlagsgesellschaft, Braunschweig/Wiesbaden, 2002.

2. V. I. Arnold. *Ordinary Differential Equations*, Springer-Verlag, Berlin, Heidelberg, 1992.

3. L.A. Bunimovich. *Mushrooms and other billiards with divided phase space* , Chaos 11, 802 - 8 (2001).

4. L.A. Bunimovich. *Relative volume of KAM tori and uniform distribution, stickiness and non stickiness in Hamiltonian systems*, Nonlinearity 21 (2008), T13 - T17.

5. G. Contopoulos. *Order and Chaos in Dynamical Astronomy*, 2nd Edition, Springer-Verlag, 2010.

6. G. Contopoulos and C. Polymilis. *Approximations of the 3-particle Toda lattice*, *Physica D***24**, 328 - 342 (1987).

7. M.C. Gutzwiller. *Chaos in Classical and Quantum Mechanics*, 1st Edition, Springer-Verlag, New York, 1990.

8. M. Hénon and C. Heiles. *The applicability of the third integral of motion: Some numerical experiments,* Astron. J. **69**, 73 - 79 (1964).

9. T. Hofmann and J. Merker. *On local Lyapunov Exponents of Chaotic Hamiltonian Systems*, CMST 24(2), 97–111 (2018).

10. G. Lansford and J. Ford. *On the stability of periodic orbits for nonlinear oscillator systems in regions exhibiting stochastic behavior, J. Math. Phys.* **13**, 700 - 706 (1972).

11. A.J. Lichtenberg and M.A. Liebermann. *Regular and Chaotic Dynamics*, Springer-Verlag, New York, 1992.

12. J.A. Nelder and R. Mead. *A Simplex Method for Function Minimization,* Computer Journal, 7: 308 - 313, 1965.

13. L.E. Reichl. *The Transition to Chaos*, 2nd Edition, Springer-Verlag, New York, 2004.

14. Ya.G. Sinai (Ed.). *Dynamical Systems, Ergodic Theory and Applications (Encyclopaedia of Mathematical Sciences, Volume 100)*, 2nd Edition, Springer-Verlag, Berlin Heidelberg, 2010.

15. D. Szász (Ed.). *Hard Ball Systems and the Lorentz Gas, (Encyclopaedia of Mathematical Sciences, Volume 101)*, 2nd Edition, Springer-Verlag, 2000.

16. I. Szücs-Csillik. *The Lie-Integrator and the Hénon - Heiles system*, Rom. Astron. J., Vol. 20, No 1, 49 - 66 (2010).

17. M. Toda. *Theory of Nonlinear Lattices*, 2nd Enlarged Edition, Springer-Verlag, Berlin Heidelberg, 1989.

18. S. Udry and L. Martinet. *Orbital behavior transition from the Hénon-Heiles to the three-particle Toda lattice Hamiltonian,* *Physica D***44**, 61 - 74 (1990).

19. Wolfram Language & System Documentation Center (2019): "SymplecticPartitionedRungeKutta" Method for NDSolve, [online] https://reference.wolfram.com/language/tutorial/NDSolveSPRK.html , [28/09/2019] .

20. H. Yoshida. *Non-integrability of the truncated Toda lattice Hamiltonian at any order*, Communications in mathematical physics, Vol. 116 Issue 4, 529–538 (1988).

21. L. Zachilas. *A review study of the 3-particle Toda lattice and higher-order truncations: The odd-order cases (part I)*, International Journal of Bifurcation and Chaos 20(10), 3007–3064 (2010).

22. L. Zachilas. *A review study of the 3-particle Toda lattice and higher-order truncations: The even-order cases (part II)*, International Journal of Bifurcation and Chaos 20(11), 3391–3441 (2010).